Determination of aerosol optical properties with lidar. A comparison between algorithms.

A.A. Floutsi

Technische Universiteit Delft

TU Delft
Delft
University of
Technology

Challenge the future

Determination of aerosol optical properties with lidar. A comparison between algorithms.

A.A. Floutsi

by

A.A. Floutsi

in partial fulfillment of the requirements for the degree of

Master of Science
in Applied Earth Sciences, track Geoscience and Remote Sensing

at the Delft University of Technology,
to be defended publicly on Wednesday May 30, 2018 at 15:00.

Supervisor:	Dr. G. Biskos,	TU Delft
Thesis committee:	Prof. dr. ir. H.W.J. Russchenberg,	TU Delft
	Prof. Dr. A. Schmidt-Ott,	TU Delft
	Ir. D. Mamali,	TU Delft

Preface

″πᾶσά τε ἐπιστήμη χωριζομένη δικαιοσύνης καὶ τῆς ἄλλης ἀρετῆς πανουργία, οὐ σοφία φαίνεται” Πλάτων, ″Μενἐξενος”, 347a

″And all knowledge, when separated from justice and virtue, is seen to be cunning and not wisdom.” Plato, ″Menexenus”, 347a

Abstract

Lidar systems can provide vertically resolved measurements of the physical and optical properties of the atmospheric particles with high spatiotemporal resolution. In this study, four case studies were analyzed and studied in order to identify the dominant aerosol type over the city of Nicosia in Cyprus: 05 April and 07 April 2015 and 17 April and 21 April 2016. More specifically, vertical profiles of the extinction and backscatter coefficient, Ångström exponent, particle linear depolarization ratio and lidar ratio were manually retrieved from the lidar signal for each case study. For the first case, the main aerosol load was observed in the very lower atmosphere, between 0.25 and 1.25 km. The observed aerosol optical properties indicated the strong presence of maritime aerosols. In the second case study, the aerosol layer was thicker and it was observed between 1.6 and 7 km. Analysis of the optical properties showed that the predominant aerosol types within the PBL were mainly maritime aerosols and aerosols from local sources while higher in the atmosphere the aerosol load consisted of dust mixtures. The third case study, on 17th April 2016, was a relatively clean day and a thin aerosol layer was observed between 0.25 and 2.0 km consisting mainly of maritime and urban aerosols. 21st of April 2016, which was the fourth case study, was a dust event case study. The aerosol load, accumulated between 2.0 and 5.0 km, was characterized as a purely dust layer. The results obtained with the manual retrieval method, were compared with automatically retrieved profiles (provided by the Leibniz Institute for Tropospheric Research) and are in good agreement. More specifically, for the vertically resolved extinction profiles at 532 nm the correlation coefficient values ranged between 0.9784 and 1. The correlation coefficients for the backscatter profiles at 532 nm and 1064 nm ranged from 0.9975 to 0.9986 and from 0.9937 to 0.9996 respectively. The linear particle depolarization ratio profiles also correlated less well with the automatically retrieved one with R ranging from 0.8781 to 0.9889 while similarly, for the volume depolarization ratio profiles the correlation coefficient ranged between 0.7054 to 0.9603.

Contents

1

Introduction

Aerosol particles interact with solar radiation, through scattering and absorption, and affect the Earth's energy balance (aerosol direct effect, [1]). Aerosols also act as cloud condensation nuclei (CCN) and ice nuclei (IN), thus altering cloud properties such as the cloud albedo, the cloud life-time etc. (aerosol indirect effect, [2]). In addition, the absorption of solar radiation by the atmospheric particles can induce local changes of the ambient temperature profile, the convection patterns and the cloud properties (aerosol semi-direct effect). This topic has been subject to many different studies, mostly due to the fact that aerosols (along with clouds) induce the biggest uncertainty to the estimates of the Earth's and atmosphere's changing energy budget. This high uncertainty is attributed to our inadequate knowledge of the spatial and temporal variability of aerosols, both their physical and chemical properties and the processes that they are involved in [3].

Although all these processes have extensively been studied during the past decades, the complete quantification of the aerosol forcing is still lacking. The aerosol radiative effect (the interaction of aerosol particles with, mainly, shortwave solar radiation), has been estimated by combining in-situ and remote sensing measurements with climate model data ([1], [4], [5], [6]). However, our knowledge on the aerosol longwave radiative effect is still limited [7]. A first step towards fully understanding the aerosol-solar radiation interactions, is to determine aerosol optical properties. Both in-situ and satellite-based measurements of the aerosol properties are valuable and contribute significantly to the reduction of this uncertainty ([8], [9]) although in-situ measurements suffer from spatial limitation.

A way to overcome this limitation is the establishment of widely implemented observational networks. Such networks are the Global Atmospheric Watch Aerosol Lidar Observation Network (GALION), which includes the European Aerosol Research Lidar Network (EARLINET, www.earlinet.org) [10], the Micro Pulse Lidar Network (MPLNET, [11]), the Asian Dust Network (ADNET, [12]) and the Aerosol

Robotic Network (AERONET, [13]) that is the principal network of ground-based aerosol observations. AERONET is a network of ground-based sun/sky radiometers, that provides total columnar aerosol properties (such as aerosol optical depth, single scattering albedo, complex refractive index, fraction of spherical particles, etc.) derived from solar radiance (both direct and scattered radiation) ([13], [14], [15], [16]).

The aforementioned aerosol effects are altitude dependent. Therefore, information about the vertical distribution of the aerosols is of high importance to the estimates of the aerosol-radiation interactions. A useful technique, commonly used within the atmospheric research community for the retrieval of vertical aerosol profiles is the Light Detection And Ranging technique (lidar). Lidar systems provide measurements of the atmospheric vertical structure with high spatiotemporal resolution and with a height range up to 100 km altitude. Vertically resolved measurements of the physical and optical properties of the atmospheric particles (i.e. particle-surface area concentration, volume and mass concentration, mean particle size and volume extinction coefficient) can be carried out with a lidar instrument [17].

The Mediterranean Sea is a region of great interest for studying the contribution of aerosols to climate, as it is a crossroad for air pollution receiving an immense variety of aerosol particles, both natural and anthropogenic [18]. The measurements used in this study were performed in Nicosia, Cyprus (35.1856°N and 33.3823°E) located in Levantine Sea, the northeastern part of the Mediterranean Sea. Cyprus' neighbouring countries are Turkey to the north, Syria and Lebanon to the east, Israel to the southeast, Egypt to the southwest and Greece to the northwest. Therefore, many different aerosol types are transported to Cyprus including desert dust from the Saharan and the Arabian desert, biomass burning aerosols from the north, fine aerosols originating from anthropogenic activities from the southeastern and maritime particles from the surrounding sea.

The aim of this study is the characterization of the different aerosol types. An effective way to do so is the retrieval and study of vertical profiles of aerosol optical properties. In this study, we use lidar datasets (elastic-backscatter lidar return signals at 355, 532 and 1064 nm). After processing the raw signals we obtain the aerosol extinction and backscatter coefficient profiles, the lidar ratio, the depolarization ratio and the Ångström exponent. The separation of fine and coarse mode particles as a function of height is essential for the aerosol characterization and therefore the POLIPHON method is applied to our data. Apart from that, backtrajectories are used to identify the origins of the aerosol particles (urban/industrial, biomass-burning, desert dust or sea salt particles) for each case study. In addition, vertically resolved optical properties of atmospheric aerosols contribute to the improvement of our understanding of the aerosol direct and indirect effects. Furthermore, the manually retrieved profiles of the aforementioned optical properties (aerosol extinction and backscatter coefficient profiles, lidar ratio, depolarization ratio and the Ångström exponent) were compared with automatically retrieved profiles provided by the Leibniz Institute for Tropospheric Research (TROPOS) and with profiles retrieved from the GARRLiC (Generalized Aerosol Retrieval from Radiometer and Lidar Combined data) algorithm (results provided by the National Observatory of Athens). These comparisons were performed in order to evaluate the existing algorithms and point out their strengths and limitations for further improvement.

The rest of the thesis is organised as follows. Chapter 2 gives an overview of the location, climate and meteorological conditions of the study region. Chapter 3 introduces the basics of lidar theory, aerosol properties, as well as the POLIPHON method and the GARRLiC algorithm. The results of the case studies and the comparisons are discussed in Chapter 4 while the summary, conclusions and an outlook for future research is given in Chapter 5.

2

Overview of the study region

This chapter gives an overview of the location and the climate in Cyprus. Apart from that, the prevailing meteorological conditions during the selected measurement days (case studies) are reported.

2.1. Cyprus: Location and Climate

Cyprus is an island in the eastern part of the Mediterranean basin (Levantine Sea basin). It is located south of Turkey, west of Syria and Lebanon, northwest of Israel, north of Egypt, and southeast of Greece (red rectangle, Fig. 2.1). Cyprus is at the crossroad of air masses coming from three different continents (Europe, Asia, and Africa), carrying desert dust aerosols originating from the Sahara desert and the deserts of the Middle East, smoke from the north (Turkey and Black Sea region) and anthropogenic particles from urban/industrial regions in southwestern Europe.

The climate of Cyprus is described as hot semi-arid Mediterranean climate (BSh and Csa) according to the Köppen climate classification. Summers (mid-May to mid-September) tend to be hot, sometimes extremely hot, and dry while winters (November to mid- March) are mild and wet. Autumn and spring are shorter, compared to summer and winter, accompanied with rapid weather changes.

The Troodos massif, located roughly in the center of the island and rising up to 1951 m, along with the Kyrenia mountain range (up to 1000 m) are strongly affecting the meteorology of Cyprus (Fig. 2.2). According to Cyprus Department of Meteorology [19], the average annual total precipitation increases with height from the southwestern windward slopes to the top of the massif (absolute change of 650 mm). Rainfall in the warmer months is negligible since the small precipitation amounts are rapidly absorbed by the hot and dry soil and evaporate almost immediately due to the high temperatures and the low humidity. Precipitation during autumn and winter shows variability. Overall, in the last 30 years

Figure 2.1: Satellite image of the study region (35.1264° N and 33.4299° E). Source: "Cyprus". **Google Earth**. November 2017.

precipitation is exhibiting a decreasing trend (decrease of 17%). On the other hand, temperature in Cyprus follows an increasing trend during the 20th century, with a rate of increase of 0.01°C per year.

Over the eastern part of the Mediterranean basin, the predominant surface winds are mostly westerly or southwesterly (winter) and northerly or northwesterly (summer), with strength ranging from light to moderate (rarely reaching gale). More specifically, over Cyprus both the wind direction and strength are quite variable due to orography and local heating effects.

2.2. Meteorological Conditions During The Case Studies

In this section, a detailed description of the meteorological conditions at Nicosia on the selected days for this analysis is given. The measurements used in the case studies presented in Ch. 4 were carried out during April 2015 and April 2016. The data presented in this section are provided by the Department of Meteorology Cyprus [19] and from radiosondes launched in weather balloons at the measurement site.

Generally, in April 2015 the weather was relatively dry with the mean temperature being slightly below the normal value (about 1.0 °C below the 30-year average, 1971-2000). For this month, a mean maximum air temperature of 23.1 °C and a mean minimum air temperature of 9.6 °C were reported. The area's average precipitation was 13.1 mm (54% of the 30-year average, 1961-1990), while the monthly precipitation was below normal in most areas (rainfall occurred only 3 times). Stable weather conditions prevailed during the analysed measurement days (05 and 07 of April 2015). Figures 2.3 and 2.4 show the atmospheric profiles (acquired by radiosondes) of temperature, pressure and relative humidity (RH) for the two case studies in 2015. As Fig. 2.3 shows, on 05 April 2015 and during the

Figure 2.2: Topographic map of Cyprus. Source: **Wikimedia Commons**. November 2017

measurement time, no temperature inversion is visible. The pressure profile follows the norm while the relative humidity is high in the lower 1 km of the atmosphere (mean profile value 49.62%±27.37). No precipitation was recorded on that day. On April 07, 2015 (Fig. 2.4) we observe a weak temperature inversion between 1 and 2 km. RH values are very high below 1 km (RH > 85%), between 1 and 2 km RH decreases rapidly, then between 2 and 5.7 km RH increases rapidly with height and finally above 5.7 km it decreases again (mean profile value 70.26%±30.39). Regardless the high RH values, no precipitation occurred on that day.

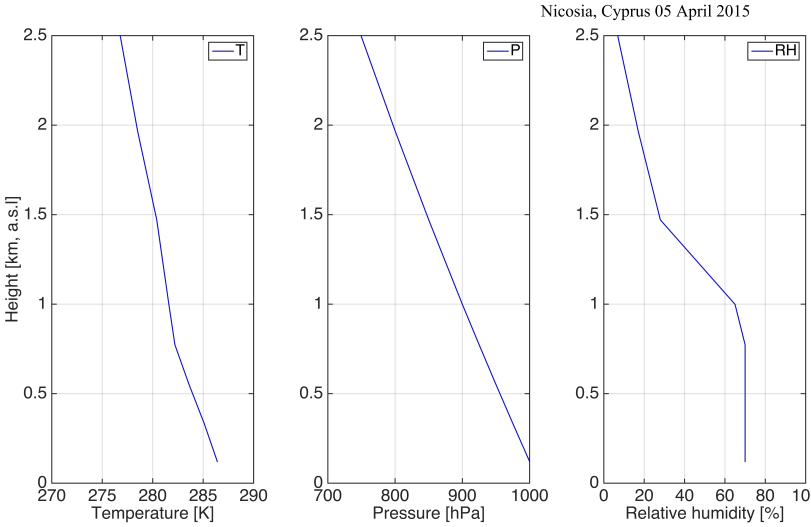

Figure 2.3: Atmospheric profiles of temperature (K), pressure (hPa) and relative humidity (%) over Nicosia at 05 April 2015, 00:00 UTC

According to Cyprus Department of Meteorology [19], the weather in April 2016 was dry and rel-

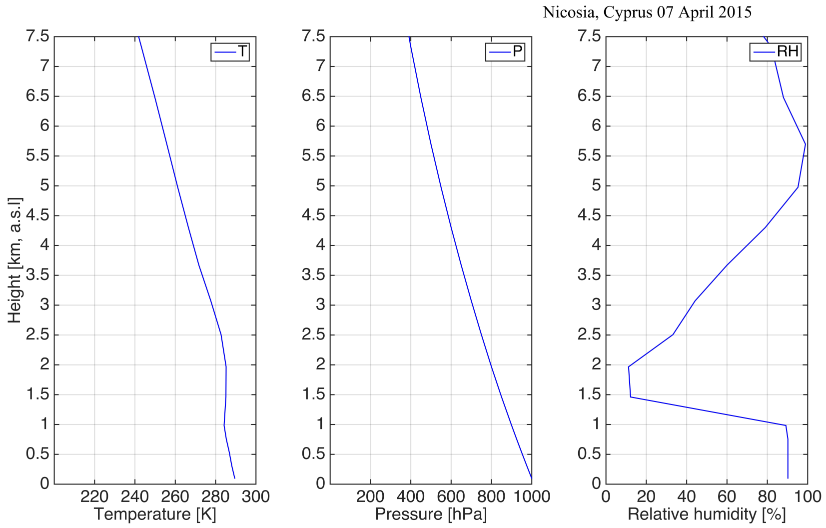

Figure 2.4: Atmospheric profiles of temperature (K), pressure (hPa) and relative humidity (%) over Nicosia at 07 April 2015, 18:00 UTC

atively warm, with the mean air temperature about 3 °C above normal (30-year average 1981-2010). For this month, the mean maximun and minumum air temperature reported was 28.9 and 13.9 °C respectively. The area average precipitation was 12.9 mm (43% of 30-year average, 1961-1990), while the monthly precipitation was below normal in most areas (rainfall occurred 3 times during April 2016). Unstable weather conditions were reported but not during the selected measurement days (17 and 21 of April 2016). Figures 2.5 and 2.6 show the radiosonde-acquired atmospheric profiles of temperature, pressure and relative humidity respectively for the aforementioned case studies. On April 17, 2016 (Fig. 2.5), a weak thermal inversion is observable between 0.82 and 1.06 km, while the mean RH value for the whole atmospheric profile is 39.57%±15.90. According to Fig. 2.6, on 21 April 2016, both the temperature and pressure profiles are normal (no temperature inversion observed). For the lowest 3 km, RH is very low (RH < 30%) and then it increases rapidly with height (mean profile value 37.24 %±31.05). For both case studies, there was no precipitation recorded.

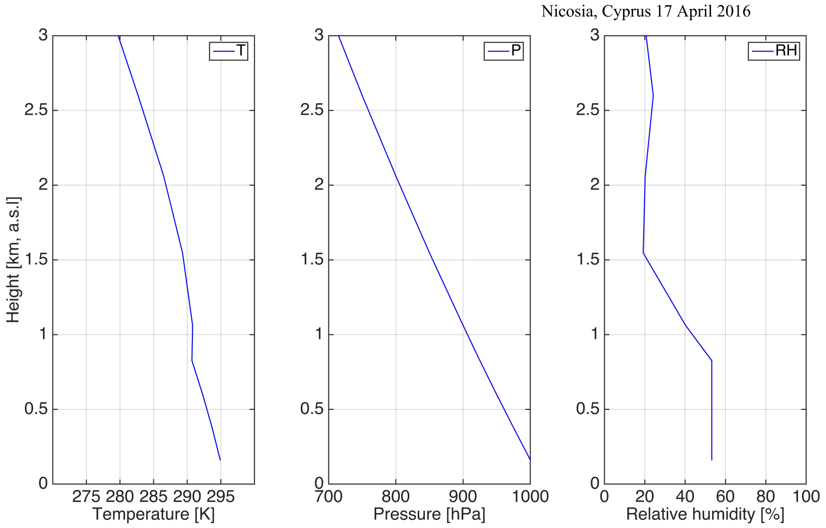

Figure 2.5: Atmospheric profiles of temperature (K), pressure (hPa) and relative humidity (%) over Nicosia at 17 April 2016, 21:00 UTC

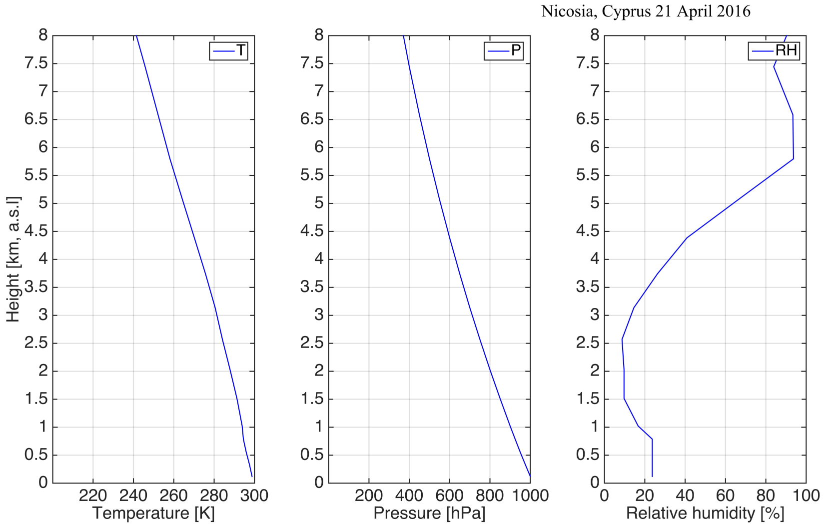

Figure 2.6: Atmospheric profiles of temperature (K), pressure (hPa) and relative humidity (%) over Nicosia at 21 April 2016, 00:00 UTC

3

Methodology

This chapter introduces the lidar profiling technique and gives an overview of the theory necessary for understanding and interpreting lidar measurements. First the lidar equation is introduced and then the backscatter and extinction coefficients follow. Two different inversion methods, namely the Klett and the Raman method are being discussed. Also, important aerosol optical and microphysical properties are explained. Finally, a brief introduction to the POLIPHON and GARRLiC algorithms, for aerosol properties retrievals, is given.

3.1. Lidar: Principles and Basic Equations

Lidar stands for Light Detection And Ranging, and is a technique based on the interaction between a laser pulse sent into the atmosphere and the different atmospheric constituents [20]. Lidar systems, emit short light pulses, generated by a laser into the atmosphere (see Fig. 3.1). A beam expander can be included within the transmitter unit, if the light beam divergence needs to be reduced, before the pulse is sent out to the atmosphere. The light pulse propagates through the atmosphere until it reaches a target and when it does, the backscattered photons are collected by a telescope at the receiver's end. Depending on the application, the optical analyzing system selects specific wavelengths and polarization states and directs the selected radiation to a detector which converts the optical measurement into an electrical signal. The intensity of the electrical signal and its dependence on the time interval between the transmission and the reception is determined electronically and stored in a computer.

Lidar observations are governed by the lidar equation:

$$P(R) = KG(R)\beta(R)T(R) \tag{3.1}$$

where P is the power received from a distance R, K is the system constant, G is the geometric factor,

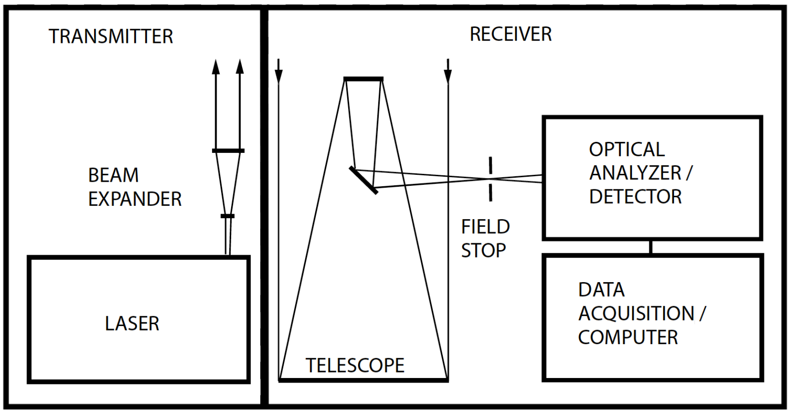

Figure 3.1: Schematics of a lidar setup. (Adapted from [17])

β is the backscatter coefficient and *T* is the transmission term (all the terms are range dependent except *K*). The system constant *K*, summarizes different parameters of the lidar system and thus it is completely determined by the lidar setup. Expanding *K* leads to:

$$K = Po\frac{c\tau}{2}A\eta \tag{3.2}$$

where *Po* is the average power of a single laser pulse, *τ* is the temporal pulse length, *A* is the telescope area and *η* is the efficiency of the system. The geometric factor *G(R)* is range dependent and along with K, is also determined by the lidar setup. *G(R)* can be written as:

$$G(R) = \frac{O(R)}{R^2} \tag{3.3}$$

where *O(R)* is the laser beam receiver field of view overlap function and *R* the range. The R^2 term is mainly responsible for the dynamic range of the lidar signal. The backscatter coefficient *β(R,λ)* describes the quantity of light that is scattered on the backward direction, and is the most important parameter determining the lidar signal strength. *β* is range and wavelength dependent and it can be written as the summation of all the types of scatterers:

$$\beta(R,\lambda) = \sum_j N_j(R)\frac{d\sigma_{j,sca}}{d\Omega}(\pi,\lambda), (m^{-1}sr^{-1}) \tag{3.4}$$

where N_j is the scattering particles concentration in the volume illuminated by the laser pulse and $d\sigma_{j,sca}/d\Omega$ the differential scattering cross section for the backward direction at a specific wavelength *λ*. Scattering in atmosphere, occurs by air molecules and aerosols and thus Eq. 3.4 can also be expressed as:

$$\beta(R,\lambda) = \beta_{mol}(R,\lambda) + \beta_{aer}(R,\lambda) \tag{3.5}$$

Nitrogen (N) and oxygen (O_2) are the primarily responsible molecules for the molecular scattering which also depends on the air density. The transmission term *T* can be expressed as:

$$T(R,\lambda) = \exp\left[-2\int_0^R a(r,\lambda)dr\right] \tag{3.6}$$

describes the total fraction of light that gets lost during the two-way transmission path and can take any value between 0 and 1. The term $\alpha(R,\lambda)$ is the extinction coefficient and is the summation of all the transmission losses. It can be defined in a similar way as the backscatter coefficient:

$$\alpha(R,\lambda) = \sum_j N_j(R)(R)\sigma_{j,ext}, (m^{-1}sr^{-1}) \tag{3.7}$$

where $\sigma_{j,ext}$ is the extinction cross section ($\sigma_{ext}(\lambda) = \sigma_{sca}(\lambda) + \sigma_{abs}(\lambda)$) in m^{-1}. In the atmosphere extinction occurs due to the light scattering and absorption by molecules and particles. Therefore, $\alpha(R,\lambda)$ can also be expressed as:

$$\alpha(R,\lambda) = \alpha_{mol,sca}(R,\lambda) + \alpha_{mol,abs}(R,\lambda) + \alpha_{aer,sca}(R,\lambda) + \alpha_{aer,abs}(R,\lambda) \tag{3.8}$$

Substitution of Eq. 3.2, 3.3 and 3.6 into Eq. 3.1, leads to the more analytical expression of the lidar equation:

$$P(R) = Po\frac{c\tau}{2}A\eta\frac{O(R)}{R^2}\beta(R)\exp\Big[-2\int_0^R a(r,\lambda)dr\Big] \tag{3.9}$$

In addition to the lidar signal *P(R)*, the background contribution P_{bg} to the recorder signal should be also be taken into account and subtracted from the data. During the daytime, the background signal is strongly affected by sunlight (direct or scattered) while at night, the moon, stars and artificial light sources contribute to the background signal. Another source of background signal is the detector noise. Finally, since the received signal intensity is inversely proportional to the range *(R)*, range correction should be applied in order to amplify the returned power. The range corrected signal is the product of the multiplication of the received signal by R^2.

3.2. Inversion Methods

The most important factors for characterizing particle optical properties are the backscatter (*β*) and the extinction (*α*) coefficients. As Eq. 3.5 and 3.7 indicate, both coefficients are range and wavelength dependent. There are two different methods that can be applied to derive the β and α profiles from lidar measurements, namely the Klett Method and the Raman Method. Both methods are discussed here, however for our analysis the Raman method was selected. The Raman method has an advantage over the Klett method: both the extinction and the backscatter coefficients are independently estimated while in the Klett method an a priori assumption of the power-law relationship of extinction and backscatter coefficients has to be made before their estimation. The latter assumption induces significant inaccuracies and possibly errors in the retrieved profiles.

3.2.1. Klett Method

The Klett Method was developed by J. D. Klett in 1981 [21]. As in previous methods, the Klett Method inverts the lidar equation (Eq. 3.9) for the extinction and backscatter coefficients [21]. A number of assumptions have to be made before the inversion. For a reference height R_0 (where the particle scattering is negligible compared to the Rayleigh scattering), a reference value for the backscatter coefficient has to be assumed. Also, the relationship between the backscatter and the extinction coefficients is assumed, since the inversion is going to be made using one equation for two different variables. The assumed relationship is a power law expressed as:

$$\beta = \text{const.} * \alpha^{k} \tag{3.10}$$

where const. and k are constant. In addition, the Klett method assumes the lidar ratio *(S)* to be constant with height, throughout the entire atmosphere. More specifically, for the 355 nm the lidar ratio is assumed to be 35, for 532 nm a value of 40 is used, while for 1064 nm the value used is 50. The last assumption corresponds to the case where there is no dispersion of the beam propagation through the atmosphere. Once all the aforementioned assumptions are made, and after solving the lidar equation, the backscatter coefficient is expressed as:

$$\beta_{aer}(R_0,\lambda) = \frac{A(R_0,R,\lambda)}{\mathrm{B}(R_0,\lambda) - 2LR_{aer}(\lambda)\int_{R_0}^{R} A(R_0,r,\lambda)dr} - \beta_{mol}(R,\lambda) \tag{3.11}$$

where

$$A(R_0,x,\lambda) = x^2 P(x,\lambda)\exp\Big[-2(LR_{aer}(\lambda) - LR_{mol})\int_{R_0}^{x}\beta_{mol}(r,\lambda)dr\Big] \tag{3.12}$$

and

$$\mathrm{B}(R_0,\lambda) = \frac{{R_0}^2 P(R_0,\lambda)}{\beta_{aer}(R_0,\lambda) + \beta_{mol}(R,\lambda)} \tag{3.13}$$

The extinction coefficient $\alpha_{aer}(R,\lambda)$ can be calculated by the following equation:

$$LR_{aer}(R,\lambda) = \frac{\alpha_{aer}(R,\lambda)}{\beta_{aer}(R,\lambda)} \tag{3.14}$$

The assumptions mentioned above induce large uncertainties in the determined aerosol extinction coefficients [22]. In contrast, in Raman lidar systems, the inelastic backscatter signal depends on the aerosol extinction and not on the aerosol backscatter, thus analysis of a single Raman lidar signal allows the determination of the aerosol extinction profile, without any crude assumptions [22].

3.2.2. Raman Method

Raman scattering (inelastic scattering) occurs when a particle, which after the interaction with the incident radiation is in the excited state, leaves that state and instead of returning to the former initial state, returns to a slightly different level. The new quantum state could be either higher or lower with respect to the former state. The Raman process (molecule's rotational and/or vibrational state change) leads to a frequency shift of the backscattered light. This alters the wavelength of the emitted radiation. Raman signal $P_R(z)$, where *z* is the distance of the target from the receiver, is expressed by the Raman lidar equation:

$$P_R(z) = \frac{K_R O_z}{z^2}\beta_R(z)\exp\left\{-\int_0^z [a_0(\zeta) + a_R(\zeta)]d\zeta\right\} \tag{3.15}$$

where O_z is the laser beam receiver field of view overlap function, K_R is a term that includes all the range-independent system parameters, $\beta_R(z)$ is the Raman backscatter coefficient, $a_o(\zeta)$ is the extinction of the light on the way to the target and $a_R(\zeta)$ is the extinction of the light on the way back to the lidar after the Raman scattering takes place. The particle extinction coefficient is defined as:

$$a_{\lambda o,aer}(z) = \frac{\frac{d}{dz}\left[\ln \frac{N_R(z)}{P_{\lambda R}(z)z^2}\right] - a_{\lambda 0,mol}(z) - a_{\lambda R,mol}(z)}{1 + (\frac{\lambda_0}{\lambda_R})^k} \tag{3.16}$$

where $N_R(z)$ is the nitrogen molecular number density and $P_{\lambda R}(z)$ is the nitrogen Raman signal as described by Ansmann et al., 1992 [23]. An assumption here is, that the particle scattering is proportional to λ^{-k}, and *k* can take different values according to the observed particles (e.g. for aerosol particles and water droplets *k* equals 1 while for ice particles k equals 0). The particle backscatter coefficients can be determined by the elastic signal $P_{\lambda 0}(z)$ and the inelastic Raman signal $P_{\lambda R}(z)$:

$$\begin{aligned} \beta_{\lambda 0,aer}(z) = {} & -\beta_{\lambda 0,mol}(z) + [\beta_{\lambda o,aer}(z_0) + \beta_{\lambda o,mol}(z_0)] \\ & \times \frac{P_{\lambda R}(z_0)P_{\lambda 0}(z)N_R(z)}{P_{\lambda 0}(z_0)P_{\lambda R}(z)N_R(z_0)} \times \frac{\exp\left\{-\int_{z} {}_{0}^{z}[a_{\lambda R,aer}(\zeta) + a_{\lambda R,mol}(\zeta)]d\zeta\right\}}{\exp\left\{-\int_{z} {}_{0}^{z}[a_{\lambda 0,aer}(\zeta) + a_{\lambda 0,mol}(\zeta)]d\zeta\right\}} \end{aligned} \tag{3.17}$$

For a more detailed description and derivations of the equations 3.15, 3.16 and 3.17 one may refer to Ansman et al., 1990 [22] and 1992 [23].

Once the backscatter and extinction coefficients are known, optical properties of atmospheric components such as the particle lidar ratio $S_{aer}(R,\lambda)$, the Ångström exponent $\alpha_{\alpha/\beta}(\lambda)$ and the linear depolarization ratio $\delta_{par}(R,\lambda)$ can be determined as described in Section 3.3.

3.3. Derivation of Aerosol Optical Parameters

The lidar ratio, or particle extinction-to-backscatter ratio, is defined simply as:

$$S_{aer}(R) = \frac{\alpha_{aer}(R)}{\beta_{aer}(R)} \tag{3.18}$$

The lidar ratio is one of the most important parameters for aerosol characterization since it depends on the size distribution, shape, and chemical composition of the observable atmospheric particles. According to the state and composition of the atmosphere, the lidar ratio can differ significantly.

The Ångström exponent, or Ångström coefficient, describes the dependency of the aerosol extinction coefficient on wavelength and it is defined as [24]:

$$A(z) = \log\left(\frac{\alpha_{\lambda 1}^{par}(z)}{\alpha_{\lambda 2}^{par}(z)}\right)/\log(\frac{\lambda_2}{\lambda_1}) \tag{3.19}$$

where $\alpha_{\lambda 1}$ and $\alpha_{\lambda 2}$ are the aerosol extinction coefficient profiles for two different wavelengths, $\lambda 1$ and $\lambda 2$, respectively. Similarly to the lidar ratio, the Ångström exponent depends on aerosol microphysical properties (size distribution, shape etc.) and on the particle's complex refractive index. More specifically, the Ångström exponent is inversely related to the particle size; the smaller the particles, the larger the exponent. In addition, it also provides information about the aerosol phase function and the aerosol radiance's relative magnitude at different wavelength.

The volume depolarization ratio is defined as the ratio of the total cross polarized to the total parallel polarized backscatter coefficient [25]:

$$\delta_{vol}(z) = \frac{\beta_{tot}^{\perp}(z)}{\beta_{tot}^{\parallel}(z)} = \frac{\beta_{aer}^{\perp}(z) + \beta_{mol}^{\perp}(z)}{\beta_{aer}^{\parallel}(z) + \beta_{mol}^{\parallel}(z)} \tag{3.20}$$

The particle linear depolarization ratio $\delta_{par}(z)$ is another important parameter for aerosol characterization since it provides information about the sphericity of the particles. In case of spherical particles, the linear depolarization ratio is close to 0, while in case of non spherical particles the depolarization ratio is greater than 0. It is defined as the ratio of the cross polarized to parallel polarized backscatter coefficient:

$$\delta_{par}(z) = \frac{\beta_{\perp}^{par}(z)}{\beta_{\parallel}^{par}(z)} \tag{3.21}$$

The particle linear depolarization ratio is a quantity that can be extracted from the volume depolarization ratio [25]:

$$\delta_{par}(z) = \frac{R\delta(\delta_{mol} + 1) - \delta_{mol}(\delta + 1)}{R(\delta_{mol} + 1) - (\delta + 1)} \tag{3.22}$$

where R is the backscatter ratio.

3.4. Aerosol Microphysical Properties Inversion Algorithms

3.4.1. POLIPHON

POLIPHON stands for POlarization LIdar PHOtometer Networking and it is a method that can be used to separate coarse and fine mode particle properties from lidar measurements. There are two variations of the method namely the one-step and the two-step POLIPHON method. In this study, the two-step POLIPHON method was applied. For more information about POLIPHON one can refer to Ansmann et al., 2012 [26], Mamouri R.E. & Ansmann A., 2014 [27] and 2016 [28].

In the two-step approach, three types of aerosol particles can be distinguished; the non-dust particles (*nd*) having a δ equal to 0.05 or less, the fine-mode dust particles (*df*) having a δ equal to 0.16 and the coarse-mode dust particles (*dc*) with a δ equal to 0.39 [27]. Initially, the backscatter coefficient attributed to the coarse-mode dust is separated from the total backscatter coefficient. The residual backscatter coefficient is the contribution of the non-dust and fine-dust particles, which is separated in the second step. The method is schematically illustrated in Fig. 3.2.

3.4.2. GARRLiC

The GARRLiC algorithm (Generalized Aerosol Retrieval from Radiometer and Lidar Combined data) uses co-located multi-wavelength elastic lidar observations and radiometer data in order to derive different aerosol parameters [29]. GARRLiC has two available configurations for either single or double mode inversion. In the single mode, the retrieved properties correspond to the total aerosol load while in

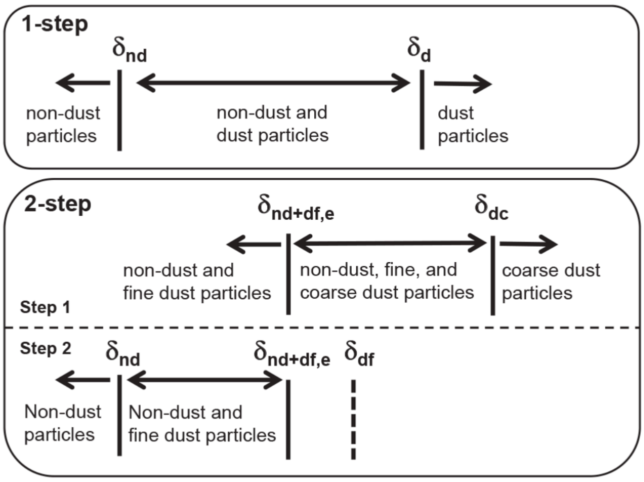

Figure 3.2: Schematic representation of the one-step (top panel) and two-step (bottom panel) POLIPHON method. (Adapted from [27])

.

the double mode properties can be retrieved for both fine and coarse mode particles. Depending on the configuration set-up and the input data, different sets of aerosol parameters and properties can be retrieved by GARRLiC. The obtained profiles are the backscatter and extinction coefficient, the volume concentration profiles, the Ångström exponent, the lidar and depolarization ratio, the single scattering albedo, the effective radius, the aerosol optical thickness, the particle size distribution, and the complex refractive index including information about both the real and the imaginary parts of the refractive index. A schematic illustration of the GARRLiC algorithm is provided in Fig. 3.3.

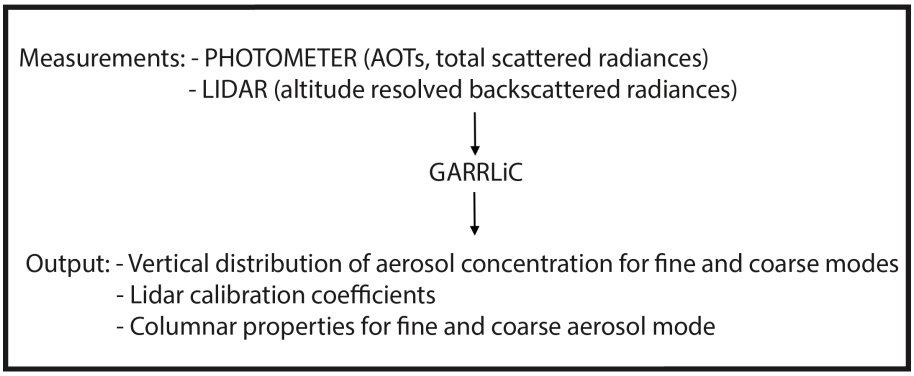

Figure 3.3: Schematic representation of the GARRLiC algorithm. (Adapted from [29])

.

4

Results

Four case studies were analyzed in detail: April 05 and April 07 in 2015 as well as April 17 and April 21 in 2016. All the case studies were carried out in the late evening by the multiwavelength-Raman-polarization lidar Polly^{XT} belonging to the National Observatory of Athens (Polly^{XT} NOA). The case studies were chosen to be quantitatively and qualitatively different, aiming to provide an overview of the typical aerosol load over Cyprus during days with low and high aerosol optical thickness.

The same methodology was followed for each case study. First the vertical profiles were retrieved manually following the Raman inversion method (see section 3.2.2). According to the observed values of lidar and depolarization ratio as well as the HYSPLIT backward trajectories an aerosol type is suggested for each case. Then, the two step POLIPHON algorithm is applied (only to the case studies with high AOT) to examine the contribution of the non-dust particles and the dust particles to the total backscatter coefficient.

4.1. Case studies

4.1.1. Case Study 1: 05 April 2015

Figures 4.1 and 4.2 show the range-corrected signal at 1064 nm and the depolarization ratio at 532 nm, respectively, on the 5th of April 2015, for the measurement period from 00:00 to 06:00 UTC. To study the background aerosol over Nicosia, we analyzed the period from 00:00 to 02:00 UTC, (indicated by a red rectangle in Fig. 4.1 and 4.2) which was chosen due to the clear sky conditions, the low aerosol load with a mean AOT value of 0.118 (500 nm) and the low depolarization ratio values. As Fig. 4.1 indicates, there is a weak signal return with an aerosol layer from 250 m up to 1250 m. No elevated aerosol layers were observed during that day. From 01:00 to 02:00 UTC, the signal becomes stronger and after 05:00 UTC as low clouds start to form (extending from 450 m up to 750 m). The depolarization ratio values are very low throughout the entire measurement period (Fig. 4.2), signifying the absence of depolarizing particles and the presence of spherical scatterers, such as maritime aerosols.

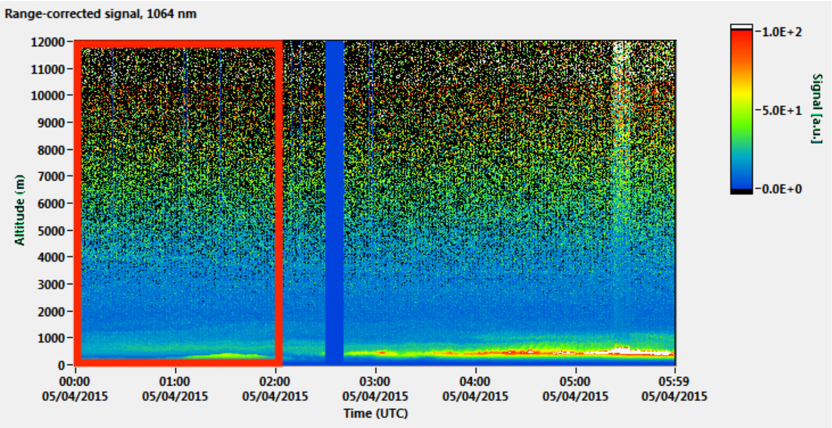

Figure 4.1: Range-corrected signal at 1064 nm recorder over Nicosia, Cyprus on April 05, 2015, from 00:00 to 06:00 UTC.

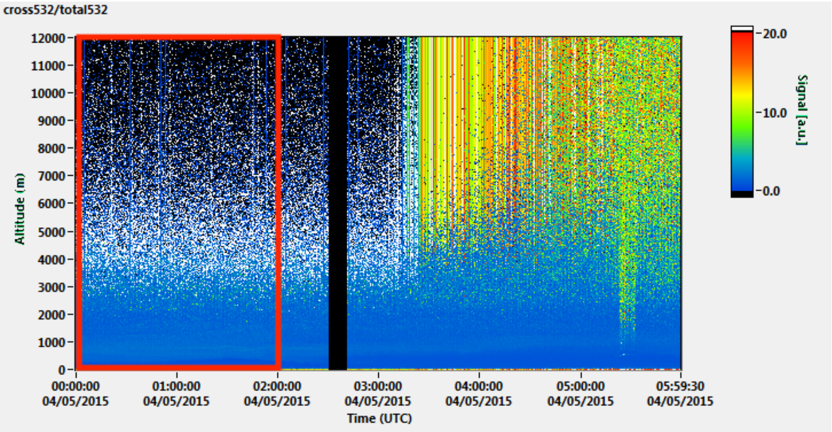

Figure 4.2: Depolarization ratio at 532 nm recorder over Nicosia, Cyprus on April 05, 2015, from 00:00 to 06:00 UTC.

Fig. 4.3 shows the retrieved profiles for the extinction coefficient (α), the backscatter coefficient (β), the Ångström exponent ($\mathring{A}$), the particle linear depolarization ratio (δ) and the lidar ratio (S) at different wavelengths. The vertical smoothing length applied to every profile, in order to decrease the signal noise, is 952.5 m. The extinction coefficient ranges between 5.29 and 23.88 Mm^{-1} at 355 nm and from 2.69 to 14.49 Mm^{-1} at 532 nm. The different behavior of the extinction profiles at 355 nm and 532 nm below 1.5 km is attributed to a technical artifact. The different wavelengths correlate well with each other for the backscatter coefficient profile, with values ranging between 0.25 and 1.34 $Mm^{-1}sr^{-1}$ at 355 nm, 0.14 and 1.01 $Mm^{-1}sr^{-1}$ at 532 nm and between 0.02 and 0.42, at 1064 nm. Between 250 m and 1250 m (where the signal is stronger) and at 532 nm, we observe moderate backscatter coefficient values with a mean of 0.62±0.22 $Mm^{-1}sr^{-1}$, relatively high Ångström exponent values with a mean of 1.60±0.23 at the wavelength pair 532/1064 nm (0.98±0.14 at 355/532 nm) and low particle linear depolarization ratio (0.09±0.01 at 355 nm and 0.08±0.00 at 532 nm). Mean lidar ratio values at 355 and 532 nm are 31.74±4.78 sr and 23.29±13.62 sr respectively. During the analyzed time period, radiosonde measurements revealed a mean relative humidity of 58.25±20.30% and this could explain the relatively high *Å* values observed. From the aforementioned information we can estimate that the aerosol load consists mainly of maritime aerosols.

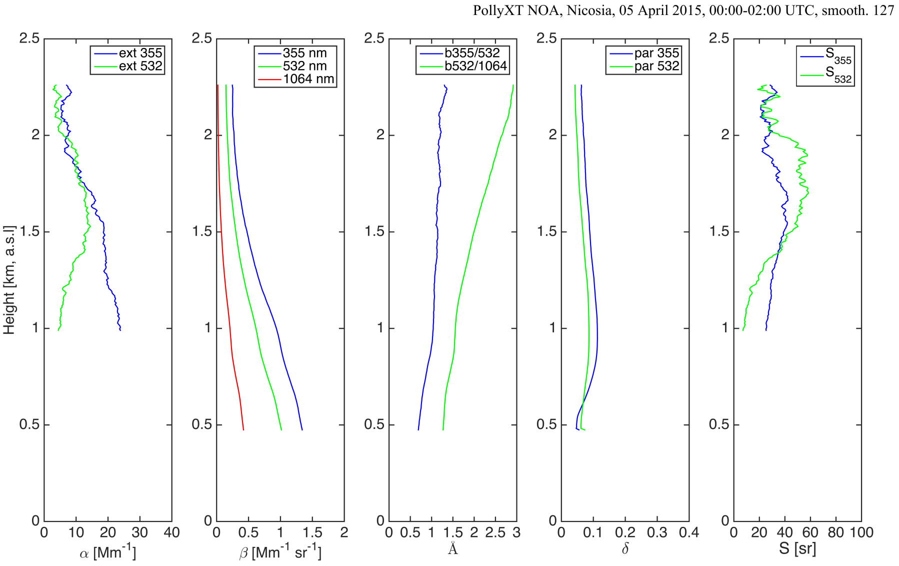

Figure 4.3: Vertical profiles of the extinction and backscatter coefficient, Ångström exponent, particle linear depolarization ratio and lidar ratio determined over Nicosia, Cyprus by the lidar measurements on April 05, 2015 from 00:00:00 to 02:00:00 UTC.

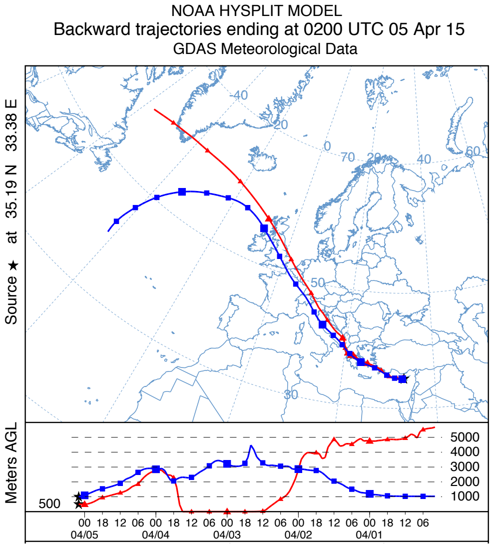

Figure 4.4: 5-day HYSPLIT backward trajectories arriving over Nicosia, Cyprus at 500 m (red line) and 1000 m (blue line) on April 05, 2015, at 01:00 UTC (http://ready.arl.noaa.gov/HYSPLIT.php).

According to the backtrajectory analysis (Fig. 4.4) all the air masses arriving at Nicosia at 01:00 UTC, originated from the northwestern Europe and the Atlantic. The air masses of the PBL (Fig. 4.4, red trajectory at 500 m) start from Greenland, cross over central Europe, along the eastern coast of Adriatic sea, then they pass over eastern and central Greece, the Aegean sea and the southwestern part of Turkey and from there they enter the Levantine sea and reach Cyprus. The air masses at 1000 m (Fig. 4.4, blue line) follow a similar pattern with the ones at 500 m starting from eastern Canada, crossing over central Europe, along the western part of Italy and then they merge with the air masses of 500 m and follow the same path. Most of the regions mentioned above are characterized by intense anthropogenic activities but they are also sources of anthropogenic dust, mainly from activities such as harvesting, ploughing, overgrazing, construction, traffic, etc. [30]. Also, since the air masses are passing over the Atlantic ocean, the Adriatic, the Aegean and the Levantine sea the presence of maritime aerosols is expected.

4.1.2. Case Study 2: 07 April 2015

The second case study corresponds to April 07, 2015, between 18:00 and 19:00 UTC. Figure 4.5 shows the range-corrected signal at 1064 nm for the whole measurement period from 18:00 to 00:00 UTC, with the study period being indicated by a red rectangle. Similarly, for the depolarization ratio at 532 nm (Fig. 4.6), a thick aerosol layer is observed between 1.6 and 7 km with the signal peaking between 2 and 4.5 km. This aerosol layer is most likely a pure dust or a mixed dust layer, due to the occurrence of a Saharan dust outbreak towards the Mediterranean Sea on April 6th (as indicated by satellite images from MODIS; data not shown here, NASA Worldview [31]). The mean AOT over Nicosia during that day was 0.204 (500 nm). Data from radiosondes (Fig. 2.4) reveal that below 1 km the RH is constant and high (90.2%), between 1 km and 2 km it decreases rapidly with height reaching 11.2% at 2 km and above 2 km increases significantly reaching up to 99% at 5.6 km.

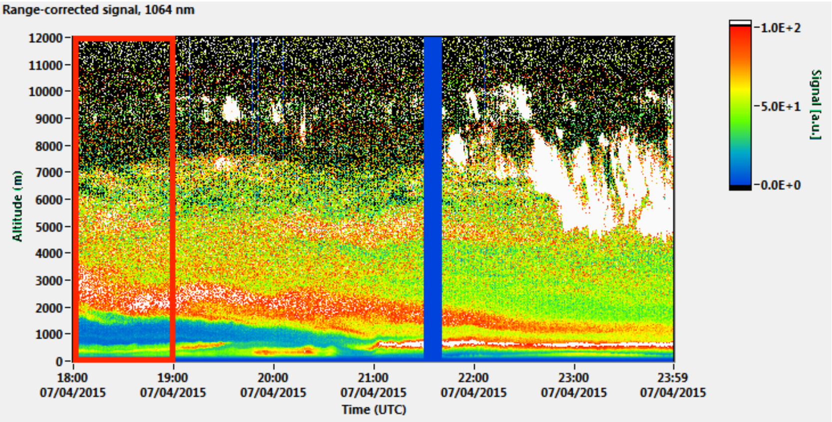

Figure 4.5: Range-corrected signal at 1064 nm recorder over Nicosia, Cyprus on April 07, 2015, from 18:00 to 00:00 UTC.

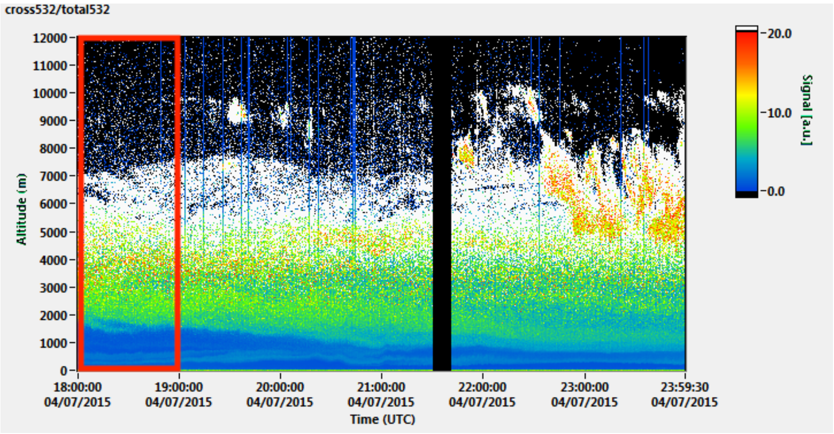

Figure 4.6: Depolarization ratio at 532 nm recorder over Nicosia, Cyprus on April 07, 2015 from 18:00 to 00:00 UTC.

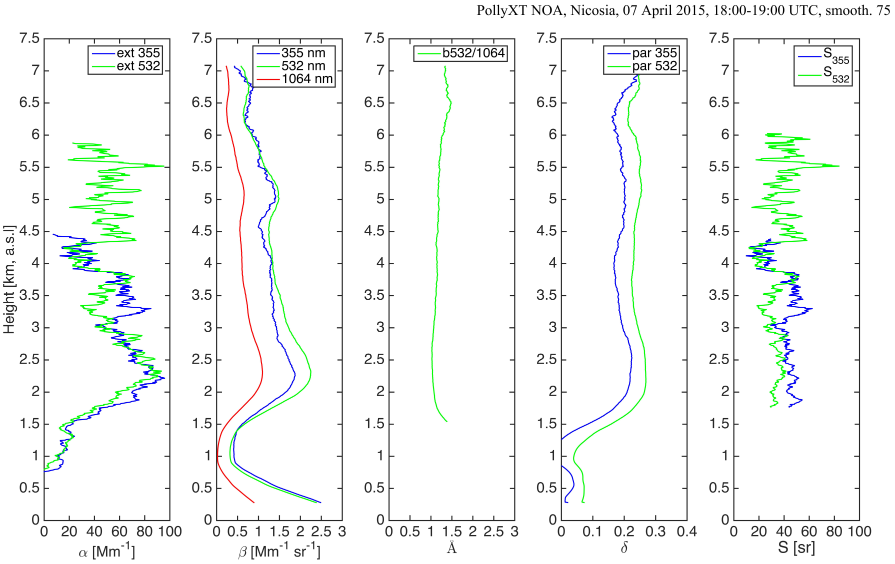

Figure 4.7: Vertical profiles of the extinction and backscatter coefficient, Ångström exponent, particle linear depolarization ratio and lidar ratio determined over Nicosia, Cyprus by the lidar measurements on April 07, 2015 from 18:00 to 19:00 UTC.

Fig. 4.7 shows the retrieved profiles for α, β, *Å*, δ and *S*. The vertical smoothing length applied to every profile is 562.5 m. The β profiles at 532 nm and 1064 nm correlate well with each other but not the one of 355 nm. This is due to technical artifacts found at the newly built instrument (Marinou E., personal communication, 2017). At 532 nm, the backscatter coefficient profile is characterized by a double maxima, one at 2.26 km (β equals to 2.25 $Mm^{-1}sr^{-1}$) and one at 5.01 km (β equals to 1.49 $Mm^{-1}sr^{-1}$), and shows wavelength independence, indicating the presence of dust. The observed β values are high, not only between 2 and 7 km where the thick aerosol layer exists (1.35 ±0.47 $Mm^{-1}sr^{-1}$), but also within the PBL. For the same region, the Å profile at 532 nm is very steady and constantly higher than 1.0, with a mean value of 1.18 ±0.12 (values associated with pure dust according to Tesche et al. [32]. The δ profile is almost constant within the entire aerosol layer and is also characterized by high values with a mean value of 0.20±0.02 at 355 nm and 0.24±0.02 at 532 nm. The lidar ratio at 532 nm exhibits a very steady behavior, with a mean value of 35.45±10.55 sr. Combining the aforementioned information we can estimate that within the PBL the predominant aerosol types are maritime aerosols and aerosols from local sources (mainly anthropogenic fine particles) while above 1.5 km dusty mixtures are dominating. Dusty mixtures (containing not only dust, but also maritime and urban aerosols) are generated by upward transport of the maritime/urban particles by turbulent mixing process.

The air masses arriving in Nicosia at 19:00 UTC during April 7, 2015, come from different directions (Fig. 4.8). The air masses of the PBL (Fig. 4.8 red trajectory line) originate from southern Italy, they cross over the Aegean sea and they are close to the surface above the southern Levantine sea and over Cyprus. Hence, the previous estimations for the predominant aerosol types within the PBL are strengthened. The air masses at 2000 m (blue trajectory line) are originating from the mid-latitudes of the Atlantic but they cross over the southernmost parts of Algeria and Tunisia before entering the regions over the Aegean and the Levantine sea and finally the area over Cyprus. Both Algeria and Tunisia are sources of desert dust particles justifying the observed β, $\mathring{A}$, δ and S values above 2 km. At 5 km (green trajectory line), the air masses originate from north Africa (Senegal, W. Sahara, Mauritania, Mali, Algeria, Tunisia), carrying desert dust particles, which explains the high aerosol load at altitudes between 5 and 7 km.

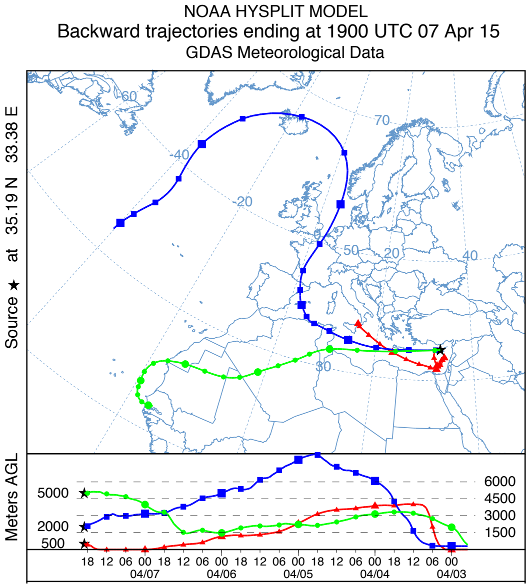

Figure 4.8: 5-day HYSPLIT backward trajectories arriving over Nicosia, Cyprus at 500 m (red line), 2000 m (blue line) and 5000 m (green line) on April 07, 2015, at 19:00 UTC (http://ready.arl.noaa.gov/HYSPLIT.php).

The aerosol types estimations based on Fig. 4.7 and Fig. 4.8 are in agreement with the POLIPHON retrieved backscatter profiles at 532 nm (Fig. 4.9). As Fig. 4.9 indicates, below 1 km the presence of non-dust particles is strong while above 1 km the predominant aerosol type is dust and more specifically coarse dust particles. This clear discrimination of the dominant aerosol types is enhanced by a temperature inversion observed at Nicosia at 19:00:00 UTC between 1 km and 1.5 km.

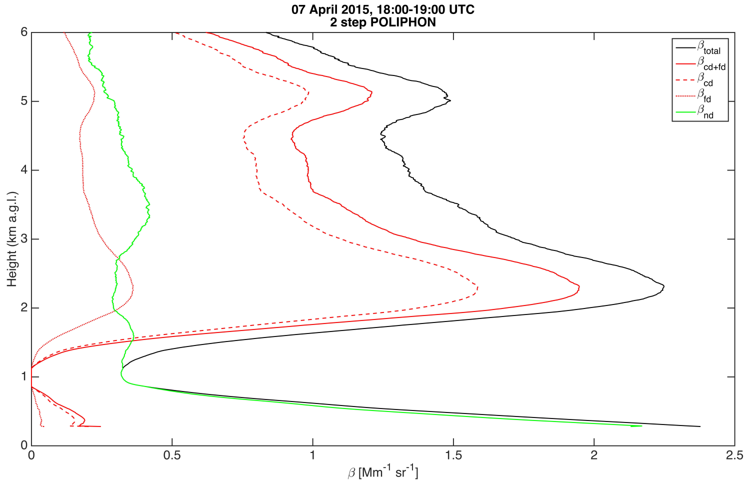

Figure 4.9: Backscatter coefficient profiles at 532 nm for the total aerosol load (black line), the coarse and fine dust fraction (red line), the coarse dust (red dashed line), the fine dust (red dotted line) and non-dust particles (green line).

4.1.3. Case Study 3: 17 April 2016

Measurements conducted on April 17, 2016, between 20:00 and 00:00 UTC were chosen as the third case study in order to characterize the background aerosol load over Nicosia. The mean AOT over Nicosia that day was 0.164 (500 nm). From the range-corrected signal at 1064 nm and the depolarization ratio at 532 nm (Fig. 4.10 and 4.11 respectively) we observe a weak signal return between 250 and 2000 m, while the radiosonde data (Fig. 2.5) show a temperature inversion between 0.82 and 1.06 km. Relative humidity on that day was low with values of 53.2% (see Fig. 2.5).

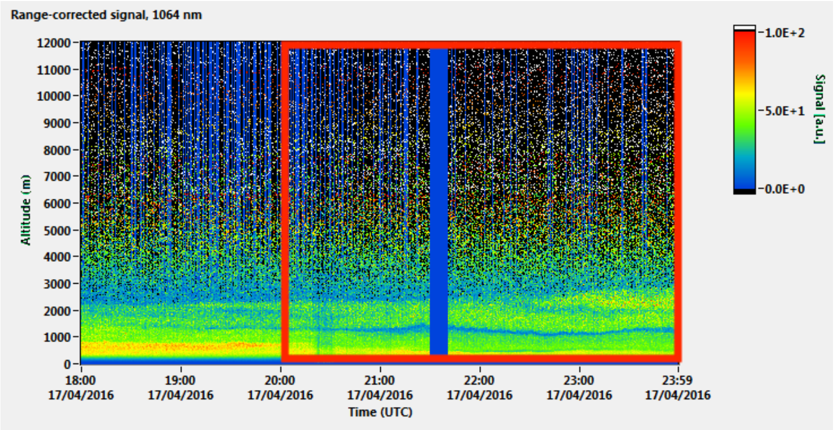

Figure 4.10: Range-corrected signal at 1064 nm recorder over Nicosia, Cyprus on April 17, 2016 from 18:00 to 00:00 UTC.

The retrieved vertical profiles for α, β, $\AA$, δ and S for this case study are shown in Fig. 4.12. The vertical smoothing length applied to every profile is 742.5 m. In this case, most of the retrieved profiles remain almost constant through the entire aerosol layer. Both the extinction profiles correlate well with each other and are steady throughout the entire aerosol layer, with a mean value of 31.03±1.95 at 355 nm and 16.48±2.13 at 532 nm. The β profiles at the three different wavelengths also show agreement,

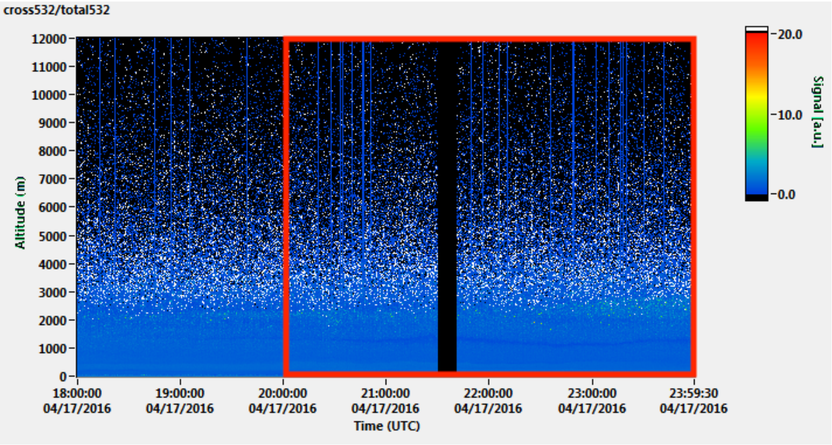

Figure 4.11: Depolarization ratio at 532 nm recorder over Nicosia, Cyprus on April 17, 2016 from 18:00 to 00:00 UTC.

with mean β value at 532 nm of 0.79±0.45 $Mm^{-1}sr^{-1}$ between 0.5 and 2 km. The $\AA$ vertical profile for the wavelength pair or 532/1064 nm has a mean value of 1.15±0.06 indicating the presence of small particles throughout the entire aerosol layer. The mean δ value at 532 nm is 0.14±0.02 (value within the range associated with dusty aerosol mixtures). The lidar ratio between 1 and 2 km has a mean value of 26.18±4.21 sr (532 nm). These values are indicating the presence of maritime and urban aerosols mixture.

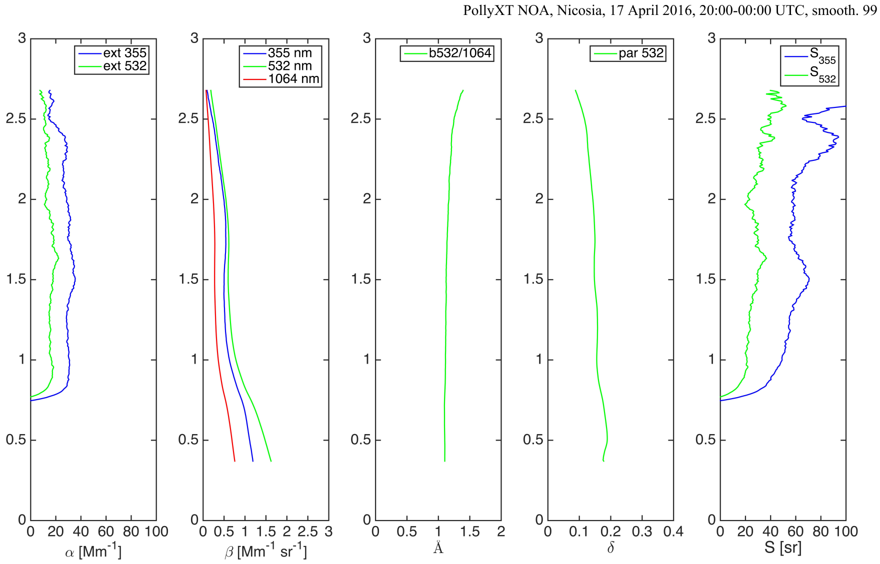

Figure 4.12: Vertical profiles of the extinction and backscatter coefficient, Ångström exponent, particle linear depolarization ratio and lidar ratio determined over Nicosia, Cyprus by the lidar measurements on April 17, 2016 from 20:00 to 00:00 UTC.

Figure 4.13 shows the 5-day HYSPLIT backward trajectories arriving over Cyprus, on the 17th of April 2016 at 00:00 UTC. The backward trajectories, arriving at 500 m (red trajectory line), 1000 m (blue trajectory line) and 2000 m (green trajectory line) are almost identical and reach back to the northwest of Cyprus. The air masses were travelling at high altitudes and started to converge over

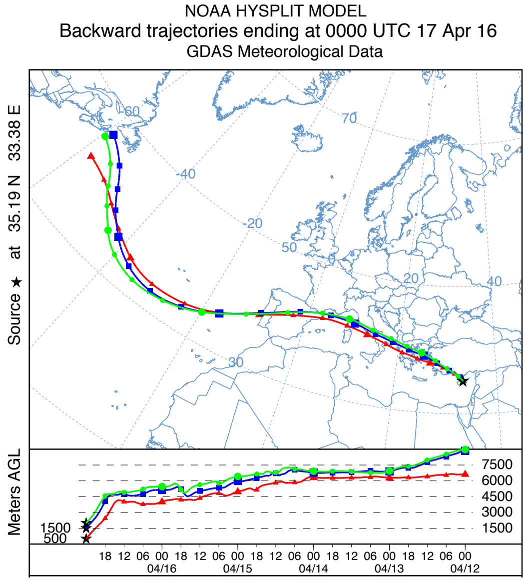

Figure 4.13: 5-day HYSPLIT backward trajectories arriving over Nicosia, Cyprus at 500 m (red line), 1000 m (blue line) and 2000 m (green line) on April 17, 2016, at 00:00 UTC (http://ready.arl.noaa.gov/HYSPLIT.php).

Levantine sea, north of Cyprus. The air masses crossed over regions characterized by strong presence of maritime and urban anthropogenic aerosol particles and therefore the results shown in Fig. 4.12 can be justified.

4.1.4. Case Study 4: 21 April 2016

The last presented case study is April 21, 2016. Between 01:00 and 01:50 UTC, we observe an elevated aerosol layer between 2.3 and 5.1 km (very strong signal shown in Fig. 4.14 and Fig. 4.15, mean AOT value of 0.351 at 500 nm). It should be noted that no temperature inversion was reported during the measurement time. Radiosonde data (Fig. 2.6) show low RH values below 2.5 km (17.45±7.10%) which are increasing rapidly above 2.5 km, with a mean value of 53.47±25.28%. The vertical smoothing length applied to every retrieved profile is 562.5 m.

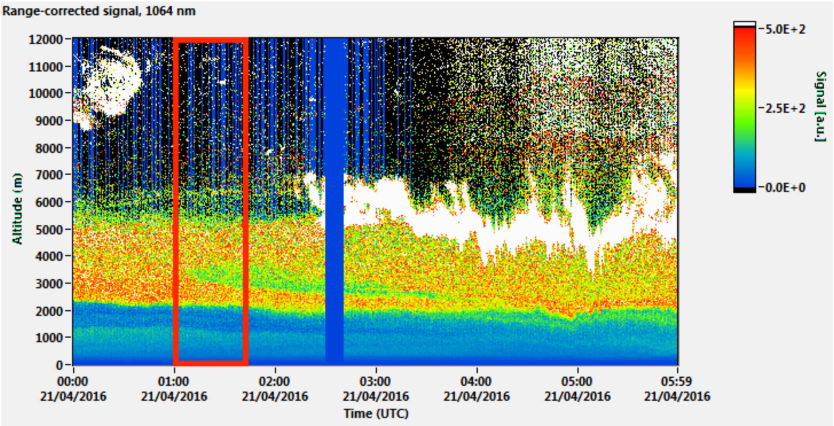

Figure 4.14: Range-corrected signal at 1064 nm recorder over Nicosia, Cyprus on April 21, 2016 from 00:00 to 06:00 UTC.

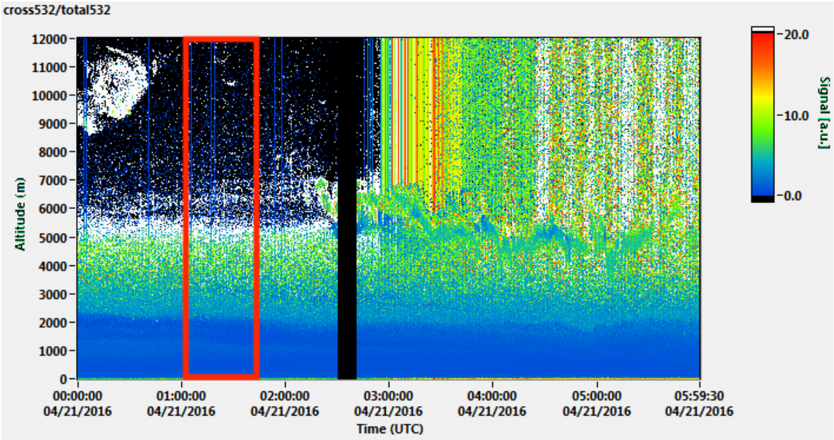

Figure 4.15: Depolarization ratio at 532 nm recorder over Nicosia, Cyprus on April 21, 2016 from 00:00 to 06:00 UTC. over Nicosia, Cyprus.

The backscatter coefficient profiles (Fig.4.16) correlate well with each other for the different wavelengths and all the profiles are characterized by a double maxima: 2.02 $Mm^{-1}sr^{-1}$ at 2.64 km and 1.92 $Mm^{-1}sr^{-1}$ at 4.68 km for 532 nm. The mean β value above 2 km and at 532 nm is high and equal to 1.55±0.40 $Mm^{-1}sr^{-1}$. The $\AA$ profile at 532 nm and within the aerosol layer is very stable and with a mean value less than 1 (0.33±0.07), indicating the presence of coarse particles. The linear depolarization ratio is also constant between 2 and 5 km with a mean value of 0.27±0.03, associating the observed aerosol layer with dust particles [33]. The mean lidar ratio at 532 nm equals 42.77±11.77 sr. The combination of δ and S, along with the $\AA$ values is typical for dust aerosol particles and therefore the observed layer between 2.3 and 5.1 km can be classified as dust layer. Within the PBL, the Ångström exponent has a mean value of 0.90±0.17 (532 nm), the mean lidar ratio is 33.58±9.81 sr (355 nm) while the linear mean depolarization ratio equals 0.13±0.02. Therefore the dominant aerosols in the PBL are small in size maritime and urban and/or smoke aerosols, most probably transferred to the area or even from local sources.

5-day backtrajectories for the same day confirm the observations discussed above (Fig. 4.17). The air masses at 500 m (red line) cross over the northern Balkans, the central Turkey and then they are close to the ground over Cyprus for the last 24 hours, indicating the presence of anthropogenic and possibly smoke particles. The air masses at 2.5 km (blue line) follow a similar pattern but this time starting from the eastern part of Spain, crossing over Po valley before entering the northern Balkans and central Turkey. Air masses were close to the ground over Egypt and Libya, collecting desert dust particles from the Sahara desert and transporting them to Cyprus, were we could observe them at high altitudes (green trajectory line).

The retrieved backscatter profiles (at 532 nm) for the total aerosol load, the coarse and fine dust and the non-dust as resulted from the application of the two-step POLIPHON method can be seen in Fig. 4.18. Below 2 km the contribution of the non-dust particles to the total backscatter coefficient is bigger than the corresponding contribution of the dust particles. There is a clear dominance of dust particles,

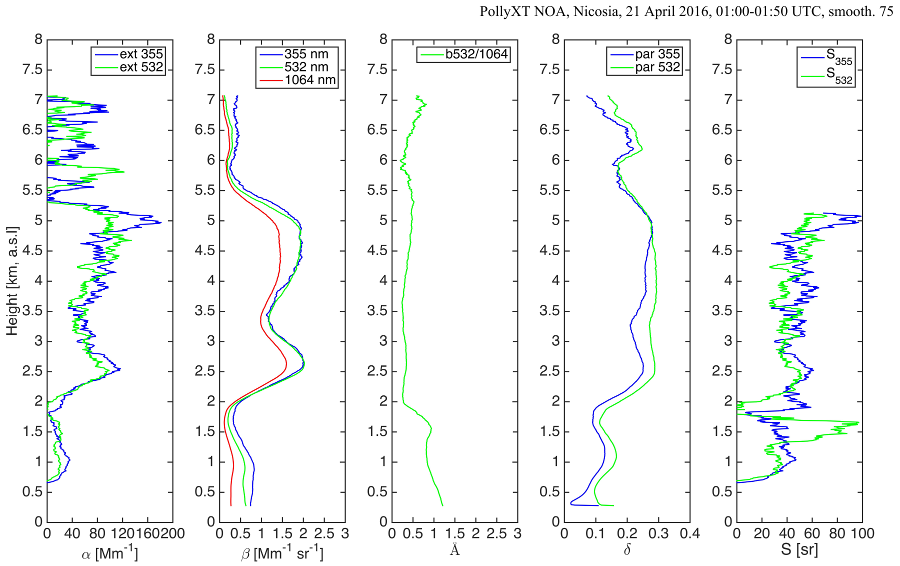

Figure 4.16: Vertical profiles of the extinction and backscatter coefficient, Ångström exponent, particle linear depolarization ratio and lidar ratio determined over Nicosia, Cyprus by the lidar measurements on April 21, 2016 from 01:00 to 01:50 UTC.

with a bigger contribution of coarse dust particles compared to the fine dust particles. However, the hygroscopic growth of the particles should be taken into account since the relative humidity reached values above 80 %.

Table 4.1 gives an overview of the analyzed case studies and the corresponding estimated aerosol types.

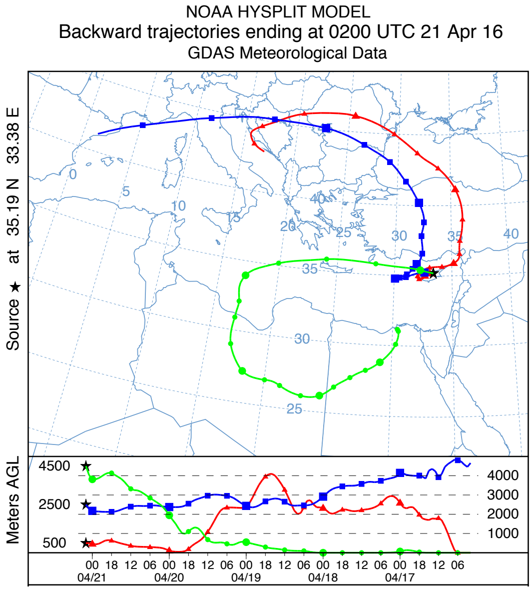

Figure 4.17: 5-day HYSPLIT backward trajectories arriving over Nicosia, Cyprus at 500 m (red line), 1000 m (blue line) and 2000 m (green line) on April 21, 2016, at 02:00 UTC (http://ready.arl.noaa.gov/HYSPLIT.php).

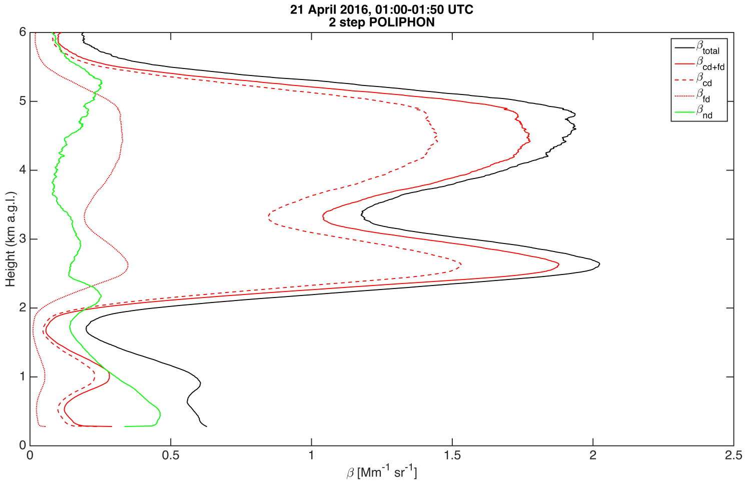

Figure 4.18: Backscatter coefficient profiles at 532 nm for the total aerosol load (black line), the coarse and fine dust fraction (red line), the coarse dust (red dashed line), the fine dust (red dotted line) and non-dust particles (green line).

Table 4.1: Overview of the case studies

Case Study	**Aerosol loading (km)**	**S (sr) at 532 nm**	**δ (532 nm)**	**Aerosol type**
05/04/2015	0.25 - 1.25	23.29±13.62	0.08±0.00	Marine
07/04/2015	1.6 - 7	35.45±10.55	0.24±0.02	Dusty Mixture
17/04/2016	0.25 - 2	26.18±4.21	0.14±0.02	Marine + Urban
21/04/2016	2 -5	42.77±11.77	0.27±0.03	Dust

4.2. Inter-comparison of the dust events

Two dust events were observed and studied in total; one on 07 April 2015 and one on 21 April 2016. Both were characterized by dense aerosol layers (indicated by the strong signal return; see Fig. 4.5 and 4.14 respectively) and high AOD values (0.204 and 0.363 at 500 nm according to AERONET). In addition, typical lidar ratio and depolarization ratio values were observed. For the first event the mean lidar ratio value was equal to 35.45±10.55 sr and the mean depolarization ratio was 0.24±0.02 (both at 532 nm) while for the second one the corresponding values were 42.77±11.77 sr and 0.27±0.03. For the first dust event (07 April 2015), backtrajectories (blue and green trajectory lines, Fig. 4.8) showed that the air masses carrying desert dust particles were originating from northwestern Africa (W. Sahara, Algeria, Tunisia). The same trajectories cross over the Aegean and Levantine sea before reaching Cyprus and thus, the observed aerosol layer was classified as dusty mixture containing both desert dust and sea salt particles. In the second case (21 April 2016), a backtrajectory within the aerosol layer (green trajectory line, Fig. 4.17) revealed that the observed aerosol layer consists mainly from desert dust particles originating from Egypt and Libya. Hence, the aforementioned aerosol layer was classified purely as a dust layer, originating from the Sahara desert.

Our results are in agreement with previous studies, following different methodologies. Moulin et al. (1998) [34], reported that over the Eastern Mediterranean basin, dust transport begins in spring and spreads over the central and western Mediterranean basins over summer at altitudes ranging from 1.8 to 9 km (Mona et al., 2006 [35]). More specifically, there is an intense and permanent dust uplift in North Africa during April, which is related to the frequent moving cyclone track (Moulin et al. (1998) [34]). During April, transferred dust in the western central basin is originating mainly from south Tunisia (Bergametti et al., 1989 [36]). For the eastern central and eastern basin and for the same month, the main dust source is the Libyan desert (Dayan et al., 1991 [37]; Kubilay and Saydam, 1995 [38]). For the far eastern Mediterranean, the major source region is the Egyptian desert (Dayan, 1986 [39]).

Nisantzi et al., 2015 [40], studied four years of observations in Cyprus (2010-2013), and he observed that desert dust particles in the region originate not only from the Sahara desert but also from the Middle East deserts. Among all the dust events in their dataset, they observed that the lidar ratio in the case of a Middle East dust outbreak had a significant difference and was lower compared with the lidar ratio observed in a Saharan dust outbreak. In the case studies studied here, the dust outbreaks were only originating from the Sahara desert and therefore we cannot draw any conclusion about the optical differences between Saharan and Middle East desert dust particles. For a statistically meaningful comparison, a longer measurement dataset would be necessary.

4.3. Comparisons between manual and automatic lidar retrievals

In this section a comparison between the manually and the automatically retrieved profiles is presented. The automated retrieval algorithm has been developed in Leibniz Institute for Tropospheric Research (TROPOS) in order to obtain the vertically resolved profiles automatically. Automatic algorithms are of great importance and are becoming more popular and favorable among the scientific community since nowadays the amount of available data is enormous compared to the actual workforce.

For the comparison we are using automatic retrieved profiles, that correspond to the aforementioned case studies, in 1 hour resolution, provided by TROPOS [41]. Therefore, the manual retrievals had to be adjusted also in 1 hour resolution (e.g. case study 3 was originally a 4 hour long measurement but it has been reduced to only 1 hour for this comparison). A vertical smoothing of 562.5 m has been applied to all the profiles. In addition, the fourth case study was also compared with profiles retrieved from GARRLiC and were provided to us by the National Observatory of Athens (NOA).

4.3.1. TROPOS Automated Algorithm

As discussed in previous chapters, a good retrieval relies upon many different factors such as the raw lidar signal and its signal-to-noise ratio, the chosen reference height, the dead time correction, the depolarization calibration etc. It is therefore crucial to make the right choices whether manual retrieval or automatic retrieval is chosen. In this thesis I examined the effect of the dead time correction to the retrieval outputs. Dead time (τ_{dead}) is defined as the time after a discrete event, during which, the system is unable to record another successive event [42]. In other words, if an event takes place during the dead time, the detector is not able to record it.

Case Study 1: 05 April 2015

In the first case study, the time interval chosen for comparison was between 01:00 and 02:00 UTC. In order to perform a sensitivity analysis and to study how the dead time correction affects the retrieval we examined the α, β, δ and volume depolarization profiles using 3 different settings for the dead-time effect. The first run was performed with no dead time correction, in the second run we used an automated dead time correction (which uses automatically coefficients of a polynomial, Baars H., personal communication, 2017) and in the last run we manually set the dead time correction to 5 ns. The same procedure has been followed for all the case studies.

Fig. 4.19 shows the comparison of the α, β, δ and volume depolarization profiles between the manually and the automatically retrieved profiles. The extinction profile of the automatic retrieval correlates well with the profiles retrieved using manual and no dead time correction. The manual (red line) and no dead time (black line) correction extinction profiles cannot be distinguished from each other on the plot because the count rates are very low, that no dead time correction is needed. The extinction profile retrieved with the automatic dead time correction is very different from the automated one up to the first 1.25 km, but from 1.25 km onward it follows the automated profile with a small positive offset. This effect might be a result of the possibly wrong polynomials used during the retrieval process with the automatic dead time correction (Baars H., personal communication, 2017). Since the automated profiles were retrieved using the no dead time correction setting, correlation coefficient values reported here correspond only to the no dead time correction profiles. As Fig. 4.19 indicates, the manually retrieved extinction profile at 532 nm correlates well with the automated one with a correlation coefficient (R) equal to 0.9995. The backscatter coefficient profiles at 532 nm and 1064 nm also correlate well with the automatically retrieved ones with correlation coefficients equal to 0.9979 and 0.9983 respectively. The offset between the automatically and manually retrieved profiles at 532 and 1064 nm is most probably due to the different reference height used. For the manual retrieval we chose a reference height from 8.0 km until 9.0 km, while the algorithm used a reference height from 2.0 km till 3.0 km. The particle and volume depolarization profiles correlate well with the automatically retrieved ones with R being equal to 0.9889 for the δ profile and 0.9603 for the volume depolarization.

Case Study 2: 07 April 2015

The time interval for the comparison in the second case study was between 18:00 and 19:00 UTC. As Fig. 4.20 demonstrates, the extinction profiles for the different retrievals are very similar with only the first 1.5 km of the manual dead time correction profile (light blue line) being different from the rest. The correlation coefficient for the automatic extinction profile and one retrieved with no dead time correction applied equals to 1.00. The backscatter profile at 532 nm and 1064 nm experiences a similar offset with the one observed in the previous case study (Fig. 4.19) again due to the different

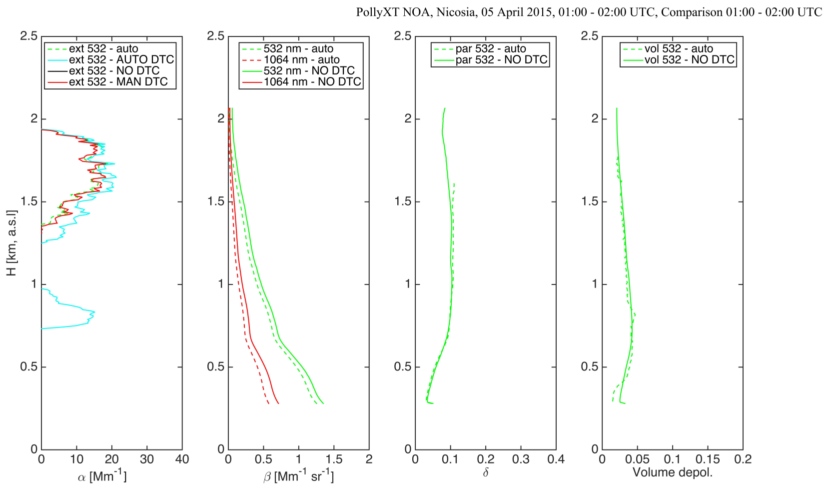

Figure 4.19: Comparison between the manually and the automatically retrieved vertical profiles of the extinction and backscatter coefficient, particle linear depolarization ratio and volume depolarization ratio over Nicosia, Cyprus on April 05, 2015, from 01:00 to 02:00 UTC.

reference heights (13.0 km - 17.0 km for the manual retrieval and 7.5 km - 8.5 km for the automatic retrieval). R for the backscatter coefficient profiles is 0.9986 and 0.9937 for the wavelengths 532 nm and 1064 nm respectively. The particle and volume depolarization profiles have an R of 0.9693 and 0.9174 respectively.

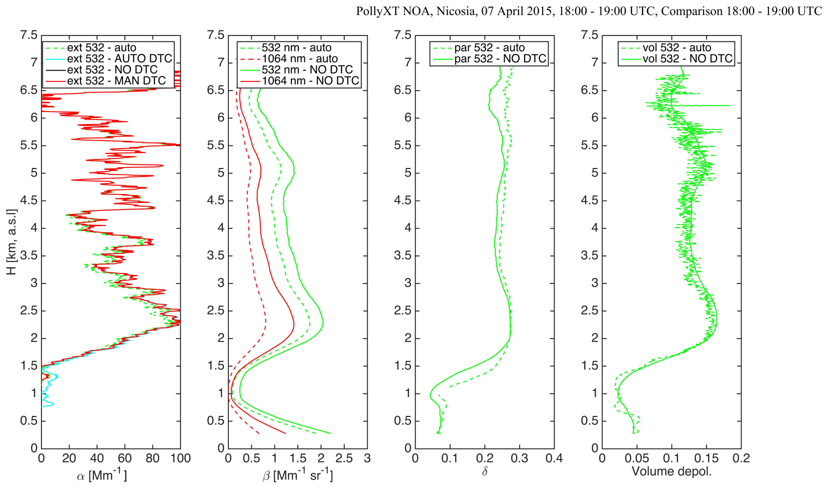

Figure 4.20: Comparison between the manually and the automatically retrieved vertical profiles of the extinction and backscatter coefficient, particle linear depolarization ratio and volume depolarization ratio over Nicosia, Cyprus on April 07, 2015, from 18:00 to 19:00 UTC.

Case Study 3: 17 April 2016

The time interval chosen for the comparison in the case of 17th of April 2016 was between 20:00 and 21:00 UTC. The theoretically aerosol-free reference height used for the manual retrieval was between 8.0 km and 10.0 km while the corresponding height determined from the algorithm for the automatic retrieval was between 2.5 km and 3.5 km.

Fig. 4.21 reveals a similar pattern with the previous case studies. The extinction profiles for all the retrievals correlate well with each other (R = 0.9994 for the automatic and the no dead time correction retrievals), with only the automatic dead time correction retrieval (light blue line) being different for the lowest 1.5 km. Backscatter profiles correlate well with respect to each other, with correlation coefficient values equal to 0.9981 and 0.9996 for 532 nm and 1064 nm respectively. As discussed before, the offset between the backscatter profiles at both 532 nm and 1064 nm is a result of the different reference heights used for the retrieval. The particle linear depolarization ratio profiles correlate well up to 1 km but above that we observe that the automatic algorithm overestimates the degree of polarization (R = 0.9322). The volume depolarization ratio from the automatically retrieved profile, is very noisy but there is a correlation with the manually retrieved profile (R = 0.7054).

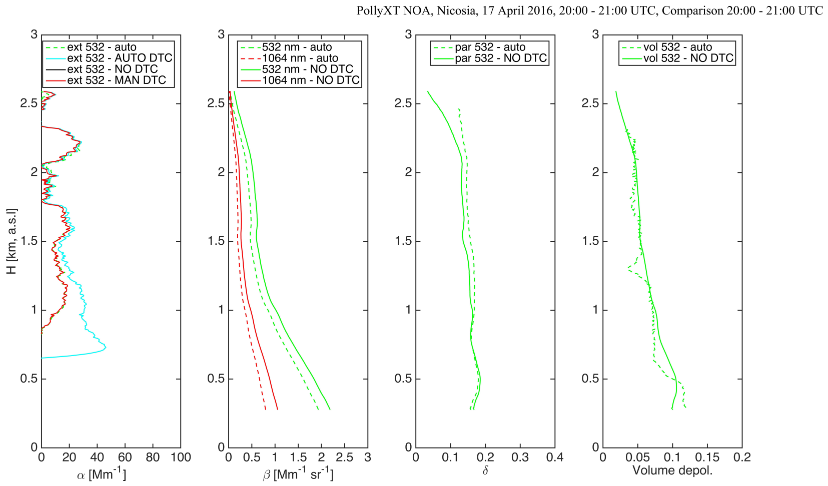

Figure 4.21: Comparison between the manually and the automatically retrieved vertical profiles of the extinction and backscatter coefficient, particle linear depolarization ratio and volume depolarization ratio over Nicosia, Cyprus on April 17, 2016 from 18:00 to 19:00 UTC.

Case Study 4: 21 April 2016

In the last case study, the manually retrieved profile on April 21, 2016 at 01:00 - 01:50 UTC was compared with the automatically retrieved one at 01:00 - 02:00 UTC. The reason for this 10 minute time difference is that after 01:50 UTC there was a small high altitude cloud in our observations. Clouds are difficult to handle manually and thus excluded. The reference height used for the manual retrieval was between 12.0 km and 14.0 km while the corresponding height for the automatic retrieval was between 5.5 km and 6.5 km.

As Fig. 4.22 indicates, the extinction profiles correlate well with each other (R = 0.9784) , with the exception of the lowest 1.5 km of the automatic dead time correction retrieved profile. The manually retrieved backscatter profile at 532 nm correlates very well with the automatically retrieved one with an R equal to 0.9980. In this case, regardless of the different reference height used, we don't observe the offset that we were observing in the previous cases. However, the algorithm failed to retrieve the backscatter profile at 1064 nm. The particle depolarization ratio profiles experience a rather big offset, with a R equal to 0.8781. The automatically retrieved volume depolarization ratio is noisy but similar with the manually retrieved one between 1.5 km and 6.0 km (R = 0.8190).

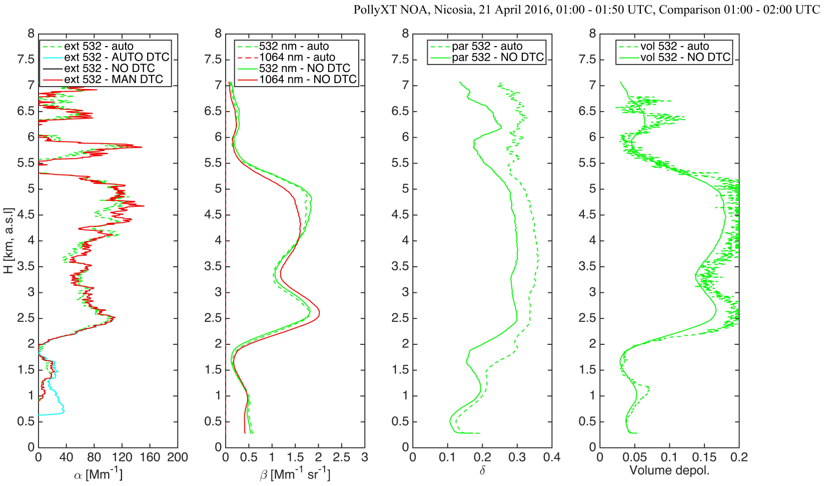

Figure 4.22: Comparison between the manually and the automatically retrieved vertical profiles of the extinction and backscatter coefficient, particle linear depolarization ratio and volume depolarization ratio for April 21, 2016 from 01:00 to 01:50 UTC over Nicosia, Cyprus.

From the cases studied above, we can conclude that the automatic retrieval algorithm performs well, with room for further improvement. The reference height is a crucial parameter for a good retrieval and thus it is necessary to be well defined by the algorithm. In some cases (e.g. 7th April 2015), the reference height set by the algorithm was very low, where there were still aerosol particles in the atmosphere. A reason for this misalignment of the height is the noisy signal, along with a high molecular contribution at some specific wavelengths which combined, result successfully passed quality tests. Another possible source for the observable differences is the manually defined settings by the user who performs the retrieval. Reference values for the extinction and the backscatter coefficients at different wavelengths and for the near field channel need to be filled in by the user. Apart from that, every time there is a neutral filter change, the calibration for the depolarization needs to be adjusted again. All the aforementioned are user-error sources and thus the improvement of the automatic retrieval algorithm is absolutely necessary.

4.3.2. GARRLiC Automated Algorithm

GARRLiC uses co-located multi-wavelength elastic lidar observations and radiometer data (see Ch. 3) and therefore the results could not be compared with the already analysed profile, which was acquired from late evening measurements. In order to make them comparable we retrieved another profile at 21 April 2016 from 12:00 till 13:30 UTC using the Klett method with a constant lidar ratio equal to 45 sr. This value, which is well within the boundaries for desert dust particles, was chosen because we have already seen the atmospheric consistency of that day (see section 4.1.4). The compared parameters in this case is the extinction and the backscatter coefficients profiles and the lidar ratio. The results from the comparison are presented in Fig. 4.23. The GARRLiC extinction profiles correlate better at a wavelength of 532 nm (R = 0.4693 for the 355 nm pair and R = 0.4803 for the 532 nm pair). However, the AOD during that day was 0.35 (at 440 nm), a value above the threshold (AOD= 0.3 at 440 nm) for acceptable particle absorption retrievals based on the ACTRIS (Aerosol, Clouds, and Trace gases Research InfraStructure) JRA1 findings (Tsekeri A., personal communication, 2017). There is an offset in the backscatter profiles as well, with the best correlation being observed again at 532 nm (R equals to 0.4719, 0.4831 and 0.4516 for 355 nm, 532 nm and 1064 nm respectively).

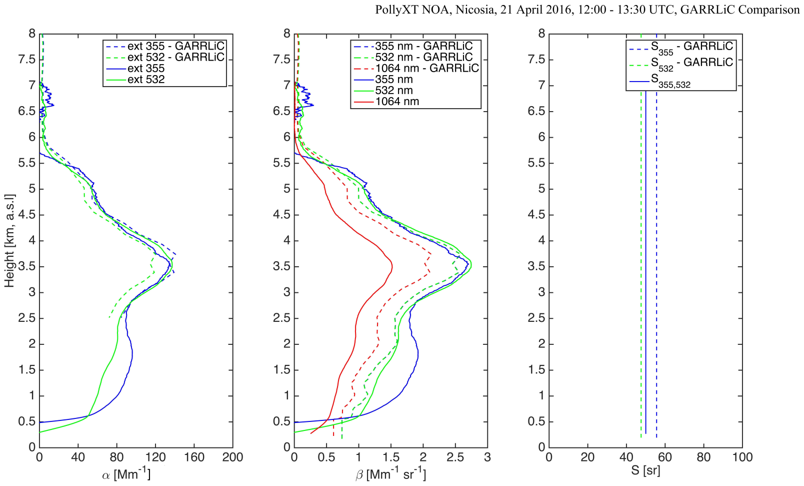

Figure 4.23: Comparison extinction, backscatter coefficient profiles and lidar ratio between a Klett and an GARRLiC retrieval.

From Fig. 4.23, the lidar depolarization measurements and the source-receptor maps (the latter two are not shown here) we can conclude that below 2.5 km the aerosol load consists mainly of dusty mixtures (dust, marine and urban particles) while above 2.5 km the predominant aerosol type is dust. However, due to a GARRLiC limitation, the results presented here consider only one mode, and that is dust particles. GARRLiC cannot retrieve well both dust and maritime particles in aerosol mixtures containing both types [43].

5

Summary, Conclusions and Outlook

5.1. Summary and conclusions

Four case studies were analyzed and studied in order to identify the dominant aerosol type over Cyprus: April 05 and April 07, 2015 and April 17 and April 21, 2016. Our analysis showed that during clean period, (AOT < 0.17), the aerosol load over Cyprus (during the month of April) is mostly comprised by marine and urban aerosols originating mostly from northwestern Europe and regions characterized by strong presence of maritime and urban anthropogenic aerosol particles. In the springtime Cyprus also experiences dust episodes, which are characterized by an increased AOT (values > 0.2). During these episodes the aerosol vertical structure is significantly different than the one corresponding to the clean period. Within the PBL, the predominant aerosol types are maritime and urban aerosols from local sources, while at higher altitudes the aerosol load is consisting of pure dust or dusty mixtures. Cyprus experiences also Middle East dust outbreaks [40], but such a dust event was not observed in the analysed case studies.

The results presented here, using the standard analysis procedure, were compared with profiles automatically retrieved by an algorithm developed in TROPOS and are in good agreement. The comparison between a manual retrieval and the GARRLiC algorithm (provided by NOA) were not so good due to the algorithm's limitations. The best correlation between the automated and the manually retrieved profiles was found in the vertically resolved profiles of the extinction and the backscatter coefficient while the correlation of linear particle and volume depolarization was less good but within the accepted range. We can conclude that the automatic retrieval algorithm performs well, with room for further improvement. For the selection of optimum reference height in the automatic algorithm should be more sophisticated in order to avoid the successful quality test passing which sometimes is a response to the accumulation of different and discrete effects. The errors induced by the user during the manual retrieval process are several and thus the improvement of the automatic retrieval algorithm is definitely necessary and desirable by the research community.

5.2. Outlook

The work psesented in this thesis contributes to the further understanding of the atmospheric aerosol transport and the processes that they get involved with using lidar observations. Furthermore, it evaluates some of the already existing retrieval methods. In order to draw more solid conclusions, however, the case studies should be extended into a timeseries. With a large enough multi-year dataset, we could be able to study in detail the year-round aerosol load over the city of Nicosia in Cyprus, as well as to examine the seasonality and the special characteristics of the dust outbreaks. Monitoring of the aerosol load and consistency over a city is very important for human health while dust events and outbreaks, originating from the Sahara and the Middle East deserts, play an important role for the climate. With accurate automatic retrievals, a huge amount of available data could be processed and studies by scientists in order to better understand the changes that atmosphere and climate undergo. The further improvement of the existing algorithms and the minimization of the errors and uncertainties in our models and observations is the ultimate key not only for a successful understanding of the current state of the atmosphere but also for accurate predictions and forecasts.

Bibliography

[1] H. Yu, Y. Kaufman, M. Chin, G. Feingold, L. Remer, T. Anderson, Y. Balkanski, N. Bellouin, O. Boucher, S. Christopher, *et al.*, *A review of measurement-based assessments of the aerosol direct radiative effect and forcing,* Atmospheric Chemistry and Physics **6**, 613 (2006).

[2] U. Lohmann and J. Feichter, *Global indirect aerosol effects: a review,* Atmospheric Chemistry and Physics **5**, 715 (2005).

[3] O. Boucher, D. Randall, P. Artaxo, C. Bretherton, G. Feingold, P. Forster, V.-M. Kerminen, Y. Kondo, H. Liao, U. Lohmann, P. Rasch, S. Satheesh, S. Sherwood, B. Stevens, and X. Zhang, *Clouds and aerosols,* in *Climate Change 2013: The Physical Science Basis. Contribution of Working Group I to the Fifth Assessment Report of the Intergovernmental Panel on Climate Change*, edited by T. Stocker, D. Qin, G.-K. Plattner, M. Tignor, S. Allen, J. Boschung, A. Nauels, Y. Xia, V. Bex, and P. Midgley (Cambridge University Press, Cambridge, United Kingdom and New York, NY, USA) Chap. 7, p. 571–658.

[4] A. Bergamo, A. Tafuro, S. Kinne, F. De Tomasi, and M. Perrone, *Monthly-averaged anthropogenic aerosol direct radiative forcing over the mediterranean based on aeronet aerosol properties.* Atmospheric Chemistry & Physics **8** (2008).

[5] C. Di Biagio, A. di Sarra, and D. Meloni, *Large atmospheric shortwave radiative forcing by mediterranean aerosols derived from simultaneous ground-based and spaceborne observations and dependence on the aerosol type and single scattering albedo,* Journal of Geophysical Research: Atmospheres **115** (2010).

[6] L. Chen, G. Shi, S. Qin, S. Yang, and P. Zhang, *Direct radiative forcing of anthropogenic aerosols over oceans from satellite observations,* Advances in Atmospheric Sciences **28**, 973 (2011).

[7] N. Bharmal, A. Slingo, G. Robinson, and J. Settle, *Simulation of surface and top of atmosphere thermal fluxes and radiances from the radiative atmospheric divergence using the arm mobile facility, gerb data, and amma stations experiment,* Journal of Geophysical Research: Atmospheres **114** (2009).

[8] N. Hatzianastassiou, B. Katsoulis, and I. Vardavas, *Sensitivity analysis of aerosol direct radiative forcing in ultraviolet–visible wavelengths and consequences for the heat budget,* Tellus B **56**, 368 (2004).

[9] N. Hatzianastassiou, C. Matsoukas, E. Drakakis, P. Stackhouse Jr, P. Koepke, A. Fotiadi, K. Pavlakis, and I. Vardavas, *The direct effect of aerosols on solar radiation based on satellite observations, reanalysis datasets, and spectral aerosol optical properties from global aerosol data set (gads),* Atmospheric Chemistry and Physics **7**, 2585 (2007).

[10] J. Bösenberg, V. Matthias, H. Linné, A. Comerón Tejero, F. Rocadenbosch Burillo, C. Pérez López, and J. M. Baldasano Recio, *Earlinet: A european aerosol research lidar network to establish an aerosol climatology,* Report. Max-Planck-Institut fur Meteorologie , 1 (2003).

[11] E. J. Welton, J. R. Campbell, T. A. Berkoff, J. D. Spinhirne, S.-C. Tsay, B. Holben, M. Shiobara, and D. O. Starr, *The micro-pulse lidar network (mpl-net),* (2002).

[12] A. Shimizu, N. Sugimoto, I. Matsui, K. Arao, I. Uno, T. Murayama, N. Kagawa, K. Aoki, A. Uchiyama, and A. Yamazaki, *Continuous observations of asian dust and other aerosols by polarization lidars in china and japan during ace-asia,* Journal of Geophysical Research: Atmospheres **109** (2004).

[13] B. N. Holben, T. Eck, I. Slutsker, D. Tanre, J. Buis, A. Setzer, E. Vermote, J. Reagan, Y. Kaufman, T. Nakajima, *et al.*, *Aeronet—a federated instrument network and data archive for aerosol characterization,* Remote sensing of environment **66**, 1 (1998).

[14] O. Dubovik and M. D. King, *A flexible inversion algorithm for retrieval of aerosol optical properties from sun and sky radiance measurements,* Journal of Geophysical Research: Atmospheres **105**, 20673 (2000).

[15] O. Dubovik, B. Holben, T. Lapyonok, A. Sinyuk, M. Mishchenko, P. Yang, and I. Slutsker, *Non-spherical aerosol retrieval method employing light scattering by spheroids,* Geophysical Research Letters **29** (2002).

[16] N. O'Neill, T. Eck, A. Smirnov, B. Holben, and S. Thulasiraman, *Spectral discrimination of coarse and fine mode optical depth,* Journal of Geophysical Research: Atmospheres **108** (2003).

[17] C. Weitkamp, *Lidar: range-resolved optical remote sensing of the atmosphere*, Vol. 102 (Springer Science & Business, 2006).

[18] J. Lelieveld, H. Berresheim, S. Borrmann, P. Crutzen, F. Dentener, H. Fischer, J. Feichter, P. Flatau, J. Heland, R. Holzinger, *et al.*, *Global air pollution crossroads over the mediterranean,* Science **298**, 794 (2002).

[19] D. of Meteorology Cyprus, *The climate of cyprus,* `http://www.moa.gov.cy/moa/ms/ms.nsf/DMLcyclimate_en/DMLcyclimate_en%3FOpenDocument`.

[20] G. Fiocco and L. Smullin, *Detection of scattering layers in the upper atmosphere (60–140 km) by optical radar,* Nature **199**, 1275 (1963).

[21] J. D. Klett, *Stable analytical inversion solution for processing lidar returns,* Applied optics **20**, 211 (1981).

[22] A. Ansmann, M. Riebesell, and C. Weitkamp, *Measurement of atmospheric aerosol extinction profiles with a raman lidar,* Optics letters **15**, 746 (1990).

[23] A. Ansmann, U. Wandinger, M. Riebesell, C. Weitkamp, and W. Michaelis, *Independent measurement of extinction and backscatter profiles in cirrus clouds by using a combined raman elastic-backscatter lidar,* Applied Optics **31**, 7113 (1992).

[24] A. Ångström, *On the atmospheric transmission of sun radiation and on dust in the air,* Geografiska Annaler **11**, 156 (1929).

[25] F. Cairo, G. Di Donfrancesco, A. Adriani, L. Pulvirenti, and F. Fierli, *Comparison of various linear depolarization parameters measured by lidar,* Applied Optics **38**, 4425 (1999).

[26] A. Ansmann, P. Seifert, M. Tesche, and U. Wandinger, *Profiling of fine and coarse particle mass: case studies of saharan dust and eyjafjallajökull/grimsvötn volcanic plumes,* Atmospheric Chemistry and Physics **12**, 9399 (2012).

[27] R.-E. Mamouri and A. Ansmann, *Fine and coarse dust separation with polarization lidar,* Atmospheric Measurement Techniques **7**, 3717 (2014).

[28] R.-E. Mamouri and A. Ansmann, *Potential of polarization lidar to provide profiles of ccn-and inp-relevant aerosol parameters,* Atmospheric Chemistry and Physics **16**, 5905 (2016).

[29] A. Lopatin, O. Dubovik, A. Chaikovsky, P. Goloub, T. Lapyonok, D. Tanré, and P. Litvinov, *Enhancement of aerosol characterization using synergy of lidar and sun-photometer coincident observations: the garrlic algorithm,* Atmospheric Measurement Techniques **6**, 2065 (2013).

[30] J. Huang, J. Liu, B. Chen, and S. L. Nasiri, *Detection of anthropogenic dust using calipso lidar measurements,* (2015).

[31] NASA, *Nasa worldview,* `https://worldview.earthdata.nasa.gov`.

[32] M. Tesche, A. Ansmann, D. Müller, D. Althausen, R. Engelmann, V. Freudenthaler, and S. Groß, *Vertically resolved separation of dust and smoke over cape verde using multiwavelength raman and polarization lidars during saharan mineral dust experiment 2008,* Journal of Geophysical Research: Atmospheres **114** (2009).

[33] V. Freudenthaler, M. Esselborn, M. Wiegner, B. Heese, M. Tesche, A. Ansmann, D. Müller, D. Althausen, M. Wirth, A. Fix, *et al.*, *Depolarization ratio profiling at several wavelengths in pure saharan dust during samum 2006,* Tellus B **61**, 165 (2009).

[34] C. Moulin, C. Lambert, U. Dayan, V. Masson, M. Ramonet, P. Bousquet, M. Legrand, Y. Balkanski, W. Guelle, B. Marticorena, *et al.*, *Satellite climatology of african dust transport in the mediterranean atmosphere,* Journal of Geophysical Research: Atmospheres **103**, 13137 (1998).

[35] L. Mona, A. Amodeo, M. Pandolfi, and G. Pappalardo, *Saharan dust intrusions in the mediterranean area: Three years of raman lidar measurements,* Journal of Geophysical Research: Atmospheres **111** (2006).

[36] G. Bergametti, A.-L. DUTOT, P. BUAT-MÉNARD, R. Losno, and E. Remoudaki, *Seasonal variability of the elemental composition of atmospheric aerosol particles over the northwestern mediterranean,* Tellus B **41**, 353 (1989).

[37] U. Dayan, J. Heffter, J. Miller, and G. Gutman, *Dust intrusion events into the mediterranean basin,* Journal of Applied Meteorology **30**, 1185 (1991).

[38] N. Kubilay and A. Saydam, *Trace elements in atmospheric particulates over the eastern mediterranean; concentrations, sources, and temporal variability,* Atmospheric Environment **29**, 2289 (1995).

[39] U. Dayan, *Climatology of back trajectories from israel based on synoptic analysis,* Journal of Climate and Applied Meteorology **25**, 591 (1986).

[40] A. Nisantzi, R.-E. Mamouri, A. Ansmann, G. Schuster, and D. G. Hadjimitsis, *Middle east versus saharan dust extinction-to-backscatter ratios,* Atmospheric Chemistry and Physics **15**, 7071 (2015).

[41] H. Baars, T. Kanitz, R. Engelmann, D. Althausen, B. Heese, M. Komppula, J. Preißler, M. Tesche, A. Ansmann, U. Wandinger, *et al.*, *An overview of the first decade of polly net: an emerging network of automated raman-polarization lidars for continuous aerosol profiling,* Atmospheric Chemistry and Physics **16**, 5111 (2016).

[42] R. L. Lucke, *Counting statistics for nonnegligible dead time corrections,* Review of Scientific Instruments **47**, 766 (1976).

[43] A. Tsekeri, A. Lopatin, V. Amiridis, E. Marinou, J. Igloffstein, N. Siomos, S. Solomos, P. Kokkalis, R. Engelmann, H. Baars, *et al.*, *Garrlic and liric: strengths and limitations for the characterization of dust and marine particles along with their mixtures,* Atmospheric Measurement Techniques **10**, 4995 (2017).